J. Fluid Mech. (2006), *vol.* 568, *pp.* 243–272.
doi:10.1017/S0022112006002023 Printed in the United Kingdom

Transient disturbance growth in a corrugated channel

By J. SZUMBARSKI[1] AND J. M. FLORYAN[2]

[1]Institute of Aeronautics and Applied Mechanics, Warsaw University of Technology, Nowowiejska 24, Warsaw, Poland, 00-665

[2]Department of Mechanical and Materials Engineering, The University of Western Ontario, London, Ontario, N6A5B9, Canada

(Received 25 March 2005 and in revised form 2 May 2006)

Transient growth of small disturbances may lead to the initiation of the laminar–turbulent transition process. Such growth in a two-dimensional laminar flow in a channel with a corrugated wall is analysed. The corrugation has a wavy form that is completely characterized by its wavenumber and amplitude. The maximum possible growth and the form of the initial disturbance that leads to such growth have been identified for each form of the corrugation. The form that leads to the largest growth for a given corrugation amplitude, i.e. the optimal corrugation, has been found. It is shown that the corrugation acts as an amplifier for disturbances that are approximately optimal in the smooth channel case but has little effect in the other cases. The interplay between the modal (asymptotic) instability and the transient growth, and the use of the variable corrugation for modulation of the growth are discussed.

1. Introduction

How surface roughness affects the laminar–turbulent transition process in shear layers is one of the fundamental questions in fluid dynamics. This question is of practical interest in several application areas, i.e. laminar airfoils, compact heat exchangers, laminar electrostatic precipitators, atmospheric boundary layers, etc. Flows over rough walls have been studied since the early works of Hagen (1854) and Darcy (1857) focused on turbulent flows; however, Reynolds (1883) was the first to pose the problem in the context of laminar-turbulent transition. In spite of many attempts (Schlichting 1979) the resolution of this problem is still incomplete.

The original experimental investigations were focused on flows in circular pipes and the various possible roughness forms were classified using the concept of 'equivalent roughness'; see Jimenez (2004) for a recent review. The phenomenological effects of the equivalent roughness are summarized in the form of the friction coefficient (Nikuradse 1933; Colebrook 1939; Moody 1944). These and other similar investigations show that surface roughness contributes directly to the dynamics of flow only if the wall is hydraulically rough. A precise definition of the hydraulical smoothness is, however, not available. While the modelling concepts of this type have been continuously re-evaluated (Bradshaw 2000; Waigh & Kind 1998), they have failed so far to uncover the mechanisms that govern the complex, flow-condition-dependent interaction between the roughness geometry and the moving fluid.

It is generally accepted that the beginning of the laminar-turbulent transition process is associated with the growth of small disturbances. The transition is a complex

nonlinear phenomenon that is initiated when disturbances reach a certain minimum threshold required to activate nonlinear effects. The initial stages of disturbance growth are described by linear theory and may have two forms. In the case of asymptotic instability, the disturbances continuously grow as a function of time and can reach an arbitrarily large magnitude that guarantees the onset of nonlinear effects. The critical conditions required for the growth, i.e. the critical Reynolds number, can be identified using linear stability theory. In the case of transient growth, the period of growth is followed by eventual decay. Determination of the largest possible growth requires solution of the initial value problem where the initial form and magnitude of the disturbance are important. The transition process may begin only if the disturbance magnitude reaches a level that is large enough to trigger secondary effects and this can be determined only through an auxiliary analysis. In summary, in this case the transition may begin only if the initial disturbance amplitude is sufficiently high.

Growth of disturbances in flow regimes covered by linearized disturbance equations and under idealized conditions has been reviewed by Schmid & Henningson (2001). The term 'idealized flow conditions' refers here to flows in quiet environments and bounded by smooth walls. Much less is known about the non-idealized situations and, in particular, about the disturbance dynamics in flows bounded by walls with distributed surface roughness. It is known from experiments that when the roughness is hydraulically 'active' the disturbance growth is explosive (Reshotko 1984; Corke, Bar Sever & Morkovin 1986). Theoretical analysis of this process is difficult as the concept of a rough wall is ill-defined and infinitely many roughness forms are possible. This leads to a paradox, as it is not possible to investigate all possible shapes. This paradox is fictitious, however, as roughness geometry can be defined in some generality in the spectral space (Floryan 1997). Analysis of the effects of different geometries is reduced in such a formulation to scans of parameter space formed by the coefficients of spectral expansions. Analysis of asymptotic instability shows that the roughness destabilizes travelling waves as well as introducing a new instability that gives rise to streamwise vortices (Floryan 1997, 2004, 2005). Analysis of different roughness shapes shows a qualitatively similar flow response as long as the spectral components of the roughness geometry are similar (Floryan 2004). A surprisingly good approximation of stability properties of flows over complex roughness shapes is obtained by working with the roughness representation truncated to the leading Fourier mode only, i.e. the wavy-wall model (Floryan 2004). Comparison of different classes of roughness shapes permits identification of conditions where surface roughness does not induce any instabilities; such roughness is referred to as hydraulically 'non-active'. A wall with 'non-active' roughness is referred to as hydraulically smooth as such roughness can induce only small changes in the flow (Floryan 2004). Small roughness is able to produce large changes only if it activates some instability processes; a wall with such roughness is referred to as hydraulically rough wall. Floryan (2004) provided criteria that identify roughness characteristics and flow conditions that guarantee that the rough wall behaves as a hydraulically smooth in the case of channel flow. Since these criteria are based only on the asymptotic instabilities, one needs to explore transient disturbance growth.

Analysis of transient disturbance growth involves solution of the initial value problem for the linear disturbance equations. In the case of a smooth wall one needs to determine the maximum possible growth at a given time, the maximum possible growth at any time, the so-called optimal growth, and the form of the initial disturbance that leads to the optimal growth, the so-called optimal disturbance. The above

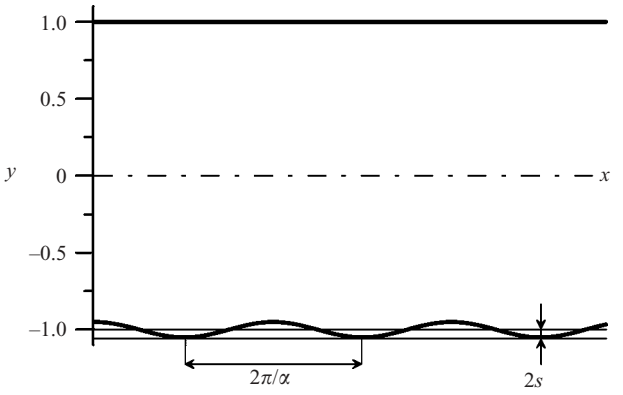

FIGURE 1. Diagram of the flow system.

questions are well-defined and the answers are well-known (Trefethen *et al.* 1993; Schmid & Henningson 2001). Similar questions need, however, to be generalized to the case of a rough wall as the growth depends on the roughness geometry. We shall define the optimal growth as the largest possible growth for a given roughness amplitude. This growth is a function of the roughness shape, which leads to the question of the identification of the shape that leads to the largest possible growth, i.e. the optimal shape or the optimal roughness. In order to avoid the paradox associated with the analysis of roughness geometry, we shall work with the spectral model. We shall provide a general formulation of the transient growth problem, but shall focus our attention and provide detailed results only on the case of the wavy-wall model which has been very successful in approximating asymptotic instability properties. All our work will be carried out in the context of two-dimensional Poiseuille flow bounded by one rough wall, which represents a convenient reference case (Floryan 2004). In § 2 we describe the form of the flow in such a channel. Linear disturbance equations are discussed in § 3. Numerical solution of these equations is discussed in § 4. The problem of determination of the maximum growth at a given time is formulated in § 4.1, the determination of the maximum growth at any time is discussed in § 4.2 and the problems of identification of the form of the optimal disturbance and the form of the optimal corrugation are formulated in § 4.3. Section 5 provides a discussion of our results.

2. Basic state

The basic state has the form of Poiseuille flow spatially modulated by the presence of wall corrugation (see figure 1). The theory describing modulation is described in detail by Floryan (1997) in the context of flow modulated by wall transpiration, and extended to the case of flow modulated by surface corrugations by Szumbarski & Floryan (1999). The description given below is limited to a short outline.

We consider steady, two-dimensional flow in a channel with a corrugated lower wall and a smooth upper wall. The flow field is represented in the form

$$\boldsymbol{V}_B(\boldsymbol{x}) = \boldsymbol{V}_0(\boldsymbol{x}) + \boldsymbol{V}_1(\boldsymbol{x}) = [u_0(y), 0] + [u_1(x, y), v_1(x, y)], \quad p_B(\boldsymbol{x}) = p_0(x) + p_1(\boldsymbol{x}), \tag{2.1}$$

where $\boldsymbol{V}_0$, p_0 describe the reference plane Poiseuille flow, $u_0 = 1 - y^2$, $p_0 = -2x/Re$, Re is the Reynolds number based on the half-channel height and the maximum

streamwise velocity, subscript B denotes basic state and $\boldsymbol{V}_1$, p_1 describe modifications associated with the presence of the corrugation. The channel extends from $-\infty$ to $+\infty$ in the x-direction and the locations of the lower and upper walls, i.e. $y_L(x)$ and $y_U(x)$, respectively, are defined as

$$y_L(x) = -1 + \left(S\,\mathrm{e}^{(\mathrm{i})\alpha x} + \mathrm{CC}\right), \quad y_U(x) = 1 \tag{2.2}$$

where CC stands for the complex conjugate. The flow is scaled using the maximum of the x-velocity of the reference Poiseuille flow and the average half-channel height.

Because of periodicity of the corrugation, the flow modifications can be represented in terms of a Fourier expansion, i.e.

$$\Psi(x, y) = \sum_{n=-\infty}^{n=+\infty} \Phi^{(n)}(y)\,\mathrm{e}^{\mathrm{i}n\alpha x}, \quad \boldsymbol{V}_1(x, y) = \sum_{n=-\infty}^{n=+\infty} \left[f_u^{(n)}(y), f_v^{(n)}(y)\right] \mathrm{e}^{\mathrm{i}n\alpha x} \tag{2.3}$$

where Ψ represents the stream function defined in the usual manner, i.e. $u_1 = \partial_y \Psi$, $v_1 = -\partial_x \Psi$, $f_u^{(n)} = \mathrm{D}\Phi^{(n)}$, $f_v^{(n)} = \mathrm{i}n\alpha\Phi^{(n)}$, $\Phi^{(n)} = \Phi^{(-n)^*}$, $f_u^{(n)} = f_u^{(-n)*}$, $f_v^{(n)} = f_v^{(-n)^*}$, $\mathrm{D} = \mathrm{d}/\mathrm{d}y$ and a star denotes complex conjugate. Elimination of pressure and use of (2.3) reduces the field equations to equations for the functions Φ_n, $n \geqslant 0$, in the form

$$\left[\mathrm{D}_n^2 - \mathrm{i}n\alpha\, Re(u_0\mathrm{D}_n - \mathrm{D}^2 u_0)\right]\Phi_n - \mathrm{i}\alpha\, Re \sum_{k=-\infty}^{k=+\infty} \left[k\,\mathrm{D}\Phi_{n-k}\mathrm{D}_k\Phi_k - (n-k)\Phi_{n-k}\mathrm{D}_k\,\mathrm{D}\Phi_k\right] = 0, \tag{2.4}$$

where $\mathrm{D}_n = \mathrm{D}^2 - n^2\alpha^2$. The boundary conditions at the channel walls are expressed in the following form:

$$u_1(x, 1) = 0, \quad v_1(x, 1) = 0, \tag{2.5a}$$

$$u_0(x, y_L(x)) + u_1(x, y_L(x)) = 0, \quad v_1(x, y_L(x)) = 0. \tag{2.5b}$$

We select the required closing condition in the form of the fixed mass flux constraint, i.e.

$$\Psi_0(1) + \Psi(x, 1) = F + Q, \tag{2.6a}$$

$$\Psi_0(y_L(x)) + \Psi(x, y_L(x)) = F, \tag{2.6b}$$

where $\Psi_0 = -y^3/3 + y + 2/3$ denotes the stream function of the Poiseuille flow (continued analytically in $-1 - 2S < y < 1$, Q stands for the (specified) volume flux and F denotes an arbitrary constant associated with the introduction of the stream function (here F denotes value of the stream function at the lower wall). In the present analysis $F = 0$ and $Q = 4/3$.

Problem (2.4)–(2.6) has been solved using spectral discretization of Φ_n based on the Chebyshev polynomials. Boundary conditions at the corrugated wall have been implemented using the immersed boundary conditions method. Details of the solution can be found in Szumbarski & Floryan (1999).

3. Linear disturbance equations

Unsteady, three-dimensional disturbances are superimposed on the basic state described previously, resulting in the total flow quantities expressed as

$$\boldsymbol{V} = \boldsymbol{V}_B(x, y) + \boldsymbol{V}_D(t, x, y, z) \tag{3.1}$$

where subscript D denotes disturbance quantities and $\boldsymbol{V}_D = [u_D(x, y, z, t), v_D(x, y, z, t), w_D(x, y, z, t)]$. Substitution of (3.1) into the vorticity transport equation and its linearization result in the following set of equations governing the evolution of disturbances:

$$\frac{\partial \boldsymbol{\omega}_D}{\partial t} + (\boldsymbol{V}_B\nabla)\boldsymbol{\omega}_D - (\boldsymbol{\omega}_D\nabla)\boldsymbol{V}_B + (\boldsymbol{V}_D\nabla)\boldsymbol{\omega}_B - (\boldsymbol{\omega}_B\nabla)\boldsymbol{V}_D = Re^{-1}\nabla^2\boldsymbol{\omega}_D, \tag{3.2a}$$

$$\boldsymbol{\omega}_B = \nabla \times \boldsymbol{V}_B, \qquad \boldsymbol{\omega}_D = \nabla \times \boldsymbol{V}_D, \qquad \nabla\cdot\boldsymbol{V}_D = 0, \tag{3.2b–d}$$

where $\boldsymbol{\omega}_B = [0, 0, \omega_{Bz}(x, y)]$ and $\boldsymbol{\omega}_D = [\omega_{Dx}(x, y, z, t),\ \omega_{Dy}(x, y, z, t),\ \omega_{Dz}(x, y, z, t)]$ denote the basic state and the disturbance vorticity, respectively. The above equations are supplemented by homogeneous boundary conditions at the lower and upper walls, i.e.

$$\boldsymbol{V}_D(t, x, y_L(x), z) = 0, \quad \boldsymbol{V}_D(t, x, 1, z) = 0. \tag{3.3}$$

Since the basic state and the shape of the lower boundary are periodic in x, the disturbances are assumed in the form (Floryan 1997)

$$\begin{aligned}\boldsymbol{V}_D(t, x, y, z) &= [\hat{u}(x, y, t), \hat{v}(x, y, t), \hat{w}(x, y, t)]\mathrm{e}^{\mathrm{i}\delta x + \mathrm{i}\beta z} \\ &= \sum_{m=-\infty}^{m=+\infty} \left[g_u^{(m)}(t, y), g_v^{(m)}(t, y), g_w^{(m)}(t, y)\right] \mathrm{e}^{\mathrm{i}(\gamma_m x + \beta z)} + \mathrm{CC}\end{aligned} \tag{3.4}$$

where β and δ are real and denote spanwise and streamwise wavenumbers, respectively, $\gamma_m = \delta + m\alpha$, and $\hat{u}$, $\hat{v}$, $\hat{w}$ describe modulation of disturbances by the corrugation and are periodic in x. Equations (3.4) and (2.3) are substituted into (3.2), and the unknowns are expressed in terms of the normal velocity component v_D and the normal vorticity component ω_{Dy}, where

$$\omega_{Dy} = \frac{\partial u_D}{\partial z} - \frac{\partial w_D}{\partial x} = -\mathrm{i}\sum_{m=-\infty}^{m=+\infty} \theta^{(m)}(t, y)\,\mathrm{e}^{\mathrm{i}(\gamma_m x + \beta z)}, \quad \theta^{(m)} = -\beta g_u^{(m)} + \gamma_m g_w^{(m)} \tag{3.5}$$

and the Fourier modes are separated resulting in the following form of the disturbance equations for $\theta^{(m)}$, $g_v^{(m)}$, $m \in (-\infty, +\infty)$:

$$\begin{aligned}&\left(\mathrm{D}^2 - k_m^2\right)\partial_t g_v^{(m)} - Re^{-1}\left\{\left(\mathrm{D}^2 - k_m^2\right)^2 - \mathrm{i}\,Re\gamma_m\left[u_0\left(\mathrm{D}^2 - k_m^2\right) - \mathrm{D}^2 u_0\right]\right\} g_v^{(m)} \\ &= Re^{-1}\sum_{n=1}^{\infty}\left(\hat{G}_v^{(m,n)} g_v^{(m+n)} + G_v^{(m,n)} g_v^{(m-n)} + \hat{G}_\theta^{(m,n)}\theta^{(m+n)} + G_\theta^{(m,n)}\theta^{(m-n)}\right) + G_v^{(0)} g_v^{(m)},\end{aligned} \tag{3.6a}$$

$$\begin{aligned}&\partial_t\theta^{(m)} - Re^{-1}\left[\mathrm{D}^2 - k_m^2 - \mathrm{i}Re\gamma_m u_0\right]\theta^{(m)} + \beta\mathrm{D}u_0 g_v^{(m)} \\ &\quad = Re^{-1}\sum_{n=1}^{\infty}\left(\hat{S}_v^{(m,n)} g_v^{(m+n)} + S_v^{(m,n)} g_v^{(m-n)} + \hat{S}_\theta^{(m,n)}\theta^{(m+n)} + S_\theta^{(m,n)}\theta^{(m-n)}\right) \\ &\qquad + S_v^{(0)} g_v^{(m)} + S_\theta^{(0)}\theta^{(m)}.\end{aligned} \tag{3.6b}$$

The explicit forms of the operators G_v, G_θ, $\hat{G}_v$, $\hat{G}_\theta$, S_v, S_θ, $\hat{S}_v$, $\hat{S}_\theta$ are given in Appendix A. The spanwise and streamwise velocity components can be easily determined from the known $\theta^{(m)}$ and $g_v^{(m)}$ using relations in the form

$$g_u^{(m)} = \frac{1}{k_m^2}\left(\mathrm{i}\gamma_m \mathrm{D} g_v^{(m)} - \beta\theta^{(m)}\right), \quad g_w^{(m)} = \frac{1}{k_m^2}\left(\mathrm{i}\beta \mathrm{D} g_v^{(m)} + \gamma_m\theta^{(m)}\right), \quad k_m^2 = \gamma_m^2 + \beta^2. \tag{3.7}$$

In the case of modal growth (asymptotic instability), when disturbances grow/decay exponentially in time, i.e. $\theta^{(m)}(t, y) = \hat{\theta}(y)\,\mathrm{e}^{-\mathrm{i}\sigma t}$, $g_v^{(m)}(y, t) = \hat{g}_v^{(m)}(y)\,\mathrm{e}^{-\mathrm{i}\sigma t}$, the above equations reduce to those given by Floryan (1997). Floryan (2003) described the vortex mode of such instability and Floryan (2005) described the travelling wave mode.

It can be shown that boundary conditions (3.3) at the upper (flat) wall take the form

$$g_u^{(m)}(t, 1) = 0, \quad g_v^{(m)}(t, 1) = 0, \quad g_w^{(m)}(t, 1) = 0, \tag{3.8a}$$

where $m \in (-\infty, +\infty)$. Boundary conditions at the lower (corrugated) wall have the form

$$\hat{u}(x, y_L(x), t) = 0, \quad \hat{v}(x, y_L(x), t) = 0, \quad \hat{w}(x, y_L(x), t) = 0, \tag{3.8b}$$

where $\hat{u}$, $\hat{v}$, $\hat{w}$ are x-periodic functions with the wavenumber α. All Fourier coefficients of these functions must be zero in order to enforce (3.8b).

Equations (3.6) with boundary conditions (3.8) form an initial value problem for the evolution of disturbances. They can be re-written as

$$\frac{\mathrm{d}\boldsymbol{H}}{\mathrm{d}t} = \boldsymbol{R}\boldsymbol{H}, \quad \boldsymbol{H}_{t=0} = \boldsymbol{H}_0, \tag{3.9}$$

where $\boldsymbol{h}^{(m)} = [g_v^{(m)}, \theta^{(m)}]^T$ describes Fourier mode m, $\boldsymbol{H} = [\ldots, h^{(-1)}, h^{(0)}, h^{(1)}, \ldots]^T$ and the form of the operator $\boldsymbol{R}$ can be easily deduced from (3.6). Solution of (3.9) can be formally written as

$$\boldsymbol{H}(t) = \mathrm{e}^{\boldsymbol{R}t}\boldsymbol{H}_0 \tag{3.10}$$

and contains complete information about the evolution of disturbances provided that we can explicitly evaluate the operator exponential. We shall discuss that issue in the next section.

Our objective is the determination of the growth of disturbances at any time t, the maximum possible growth and the initial form of disturbances that produce such growth and the time when such growth occurs and, finally, the optimal form of the corrugation, i.e. the amplitude and the wavenumber of the corrugation that leads to the largest growth. When corrugation amplitude is zero, operator $\boldsymbol{R}$ has non-zero entries only on the diagonal and the $h^{(m)}$ describe the evolution of disturbance subsets characterized by streamwise wavenumbers $\delta + m\alpha$, $m \in (-\infty, +\infty)$ that are decoupled from each other. Schmid & Henningson (2001) discussed the transient (non-modal) growth of such disturbances. When corrugation amplitude is non-zero, all the $h^{(m)}$ form a coupled system with the non-zero entries on the off-diagonals of $\boldsymbol{R}$. This coupling occurs due to the right-hand sides of (3.6) associated with the spatial structure of the flow field and due to the boundary conditions (3.8a) associated with the shape of the wall. The transient growth in this case may occur due to the non-normality within each disturbance subset as well as due to the possible non-orthogonality between such subsets.

In the present analysis we use the kinetic energy E_k of disturbances defined as

$$E_k(t) = \frac{1}{4\lambda_z} \lim_{L\to\infty} \frac{1}{L} \int_0^{\lambda_z} \int_{y_L}^{1} \int_{-L/2}^{L/2} \left(u_D^2 + v_D^2 + w_D^2\right) \mathrm{d}x\,\mathrm{d}y\,\mathrm{d}z \tag{3.11}$$

as a measure of disturbance magnitude, where $\lambda_z = 2\pi/\beta$. The limiting process in the x-direction is required as the disturbance/corrugation system is not periodic in general. When the ratio of α and δ is rational, L stands for the periodicity of this system that is dictated by the smallest common denominator of α and δ; the limiting process is not required in this case.

4. Discretization process and numerical solution

This section a provides discussion of the methodology used in the explicit evaluation of the formal solution (3.10). We begin with the solution in the form given by (3.4), truncate it at $-M, \ldots, +M$ terms and express the unknowns in terms of Chebyshev expansions in the form

$$g_v^{(m)}(t, y) = \sum_{k=0}^{k=K_v} \Gamma_k^m(t)\, \hat{T}_k(y), \quad \theta^{(m)}(t, y) = \sum_{k=0}^{k=K_\theta} \Xi_k^m(t)\, \hat{T}_k(y) \tag{4.1}$$

where the Chebyshev polynomials $\hat{T}(y)$ are defined in the complete computational domain $y \in (-1-2S, 1)$ as required by the implementation of the immersed boundary conditions concept; they are related to the standard polynomials using relation $\hat{T}_k(y) = T_k[(y+S)/(1+S)]$. Evolution equations for the time-dependent expansion coefficients can be written as

$$\boldsymbol{Q}\frac{\mathrm{d}\boldsymbol{\eta}}{\mathrm{d}t} = -\mathrm{i}\boldsymbol{P}\boldsymbol{\eta} \tag{4.2a}$$

where $\boldsymbol{\eta}(t) = [\Gamma_0^m(t), \ldots, \Gamma_{K_v}^m(t);\ \Xi_0^m(t), \ldots, \Xi_{K_\theta}^m(t)]^T$, $m = -M, \ldots, 0, \ldots, M$, subject to boundary conditions

$$\boldsymbol{B}\boldsymbol{\eta} = 0. \tag{4.2b}$$

The solution utilizes $(K_v + K_\theta + 2)$ polynomials with the differential equation (4.2*a*) used to construct algebraic equations for the first $(K_v - 4)$ coefficients Γ^m and the first $(K_\theta - 2)$ coefficients Ξ^m for each m, leading to $(2M+1)(K_v + K_\theta - 4)$ algebraic equations. Matrix $\boldsymbol{B}$ includes $3^*(2^*M+1)$ linear relations among $\Gamma_k^m, \Xi_k^m, k = 0, 1, 2, \ldots, m = \ldots, -1, 0, 1, \ldots$ resulting from the implementation of the immersed boundary conditions at the lower wall and $3^*(2^*M+1)$ conditions expressing standard conditions at the upper wall (Szumbarski 2002; Floryan 2002).

In the case of modal growth, $\boldsymbol{\eta}(t) = \boldsymbol{z}\,\mathrm{e}^{-\mathrm{i}\sigma t}$ and one obtains a generalized eigenvalue problem in the form

$$\hat{\boldsymbol{P}}\boldsymbol{z} = \sigma\hat{\boldsymbol{Q}}\boldsymbol{z} \tag{4.3}$$

where

$$\hat{\boldsymbol{P}} = \begin{bmatrix}\boldsymbol{P}\\ \boldsymbol{B}\end{bmatrix}, \quad \hat{\boldsymbol{Q}} = \begin{bmatrix}\boldsymbol{Q}\\ \boldsymbol{0}\end{bmatrix}.$$

Transient growth problem can be written in an analogous manner in the form

$$\frac{\mathrm{d}\boldsymbol{\eta}}{\mathrm{d}t} = -\mathrm{i}\boldsymbol{A}\boldsymbol{\eta}, \quad \boldsymbol{A} = \begin{bmatrix}\boldsymbol{Q}\\ \boldsymbol{B}\end{bmatrix}^{-1}\begin{bmatrix}\boldsymbol{P}\\ \boldsymbol{0}\end{bmatrix} \tag{4.4a}$$

subject to initial conditions

$$\boldsymbol{\eta}(0) = \boldsymbol{\eta}_0. \tag{4.4b}$$

It is assumed that the initial conditions are consistent with the field equations and satisfy boundary conditions ($\boldsymbol{B}\boldsymbol{\eta}_0 = 0$). The solution of (4.4) has the form

$$\boldsymbol{\eta}(t) = \mathrm{e}^{-\mathrm{i}\boldsymbol{A}t}\boldsymbol{\eta}_0. \tag{4.5}$$

The operator exponential provides complete information about the disturbance evolution. We begin explicit evaluation of this operator by the eigenvalue decomposition of $\boldsymbol{A}$, i.e. $\boldsymbol{A} = \boldsymbol{V}\boldsymbol{\Lambda}\boldsymbol{V}^{-1}$ where $\boldsymbol{\Lambda}$ denotes the diagonal matrix of eigenvalues and $\boldsymbol{V}$ denotes the corresponding eigenvectors. We assume that the set of eigenvectors of $\boldsymbol{A}$ is complete but the formal proof needs to be carried as in the case of the smooth

channel (DiPrima & Habetler 1969). The operator $\boldsymbol{A}$ may, in general, have degenerate eigenvalues and thus one would need to include generalized eigenfunctions. It is known that in the case of smooth channel the form of optimal disturbances varies smoothly across the degeneracy (Reddy & Henningson 1993) and thus an accurate representation of the solution close to the degeneracy can be obtained using regular eigenvalues. Results discussed in § 5 confirm that this does indeed occur in the case of a corrugated channel; however, formal analysis of the degenerate case remains to be carried out.

The solution can be written as

$$\boldsymbol{\eta}(t) = \boldsymbol{V}\,\mathrm{e}^{-\mathrm{i}\boldsymbol{\Lambda}t}\boldsymbol{V}^{-1}\boldsymbol{\eta}_0, \qquad \mathrm{e}^{-\mathrm{i}\boldsymbol{\Lambda}t} = \mathrm{diag}\,\{\mathrm{e}^{-\mathrm{i}\sigma_1 t}, \ldots, \mathrm{e}^{-\mathrm{i}\sigma_{\mathrm{dim}A}t}\}, \tag{4.6}$$

and can be evaluated without any difficulty at any instant of time. Only N leading eigenfunctions are used in the calculations, where N is established through numerical experimentation to provide the desired accuracy for quantities of interest (see § 4.4). We shall measure the magnitude of disturbances using kinetic energy E_k the evaluation of which is explained in Appendix B. For convenience, we shall introduce energy norm of the solution

$$\|\boldsymbol{\eta}\|_E := \sqrt{E_k} = \sqrt{\boldsymbol{\eta}^H \boldsymbol{E}\boldsymbol{\eta}} \tag{4.7}$$

where the explicit form of the symmetric, positive definite matrix $\boldsymbol{E}$ is given in Appendix B.

4.1. *Maximum growth at a specified time*

It is of interest to determine the maximum possible growth of disturbances characterized by the wavenumbers δ and β at a given time $t = \tau > 0$ and the corresponding initial conditions. This problem can be formally posed as finding the maximum value of $\|\boldsymbol{\eta}(\tau)\|_E$ at time τ over all possible initial conditions $\boldsymbol{\eta}(0)$ subject to normalization $\|\boldsymbol{\eta}(0)\|_E = 1$. This is an optimization problem representing a special case of a more general problem, i.e. the problem of finding vector $\boldsymbol{\chi}$ which gives the maximum of $\boldsymbol{J}(\boldsymbol{\chi}) \equiv \boldsymbol{\chi}^H \boldsymbol{G}\boldsymbol{\chi}$ subject to constraint $L(\boldsymbol{\chi}) \equiv \boldsymbol{\chi}^H \boldsymbol{J}\boldsymbol{\chi} = 1$, where $\boldsymbol{G}$ and $\boldsymbol{J}$ are symmetric positive definite, $\boldsymbol{\chi} \in C^N$ and N defines the size of the matrices.

The solution (4.6) can be written in the form

$$\boldsymbol{\eta}(t) = \boldsymbol{V}\,\mathrm{e}^{-\mathrm{i}\boldsymbol{\Lambda}t}\boldsymbol{w} \quad \text{where} \quad \boldsymbol{w} = \boldsymbol{V}^{-1}\boldsymbol{\eta}_0. \tag{4.8}$$

The energy norm can be written as

$$\|\boldsymbol{\eta}(\tau)\|_E^2 = \boldsymbol{w}^H \boldsymbol{M}(\tau)\boldsymbol{w} \quad \text{where} \quad \boldsymbol{M}(\tau) = \mathrm{e}^{\mathrm{i}\boldsymbol{\Lambda}^H\tau}\boldsymbol{V}^H\boldsymbol{E}\boldsymbol{V}\,\mathrm{e}^{-\mathrm{i}\boldsymbol{\Lambda}\tau} \tag{4.9a}$$

The constraint for the initial energy has the form

$$\|\boldsymbol{\eta}_0\|_E^2 = \boldsymbol{w}^H \boldsymbol{M}_0 \boldsymbol{w} = 1 \quad \text{where} \quad \boldsymbol{M}_0 \equiv \boldsymbol{M}(0) = \boldsymbol{V}^H\boldsymbol{E}\boldsymbol{V}. \tag{4.10a}$$

To solve the constrained optimization problem we follow the approach used by Butler & Farrell (1992). The extended functional for this problem can be defined as

$$\Phi(w) = \boldsymbol{w}^H \boldsymbol{M}(\tau)\boldsymbol{w} - \varepsilon[\boldsymbol{w}^H \boldsymbol{M}_0 \boldsymbol{w} - 1] \tag{4.11a}$$

where ε is the Lagrange multiplier for the fixed initial energy. The Euler–Lagrange equation for this functional can be written in the form of the following eigenvalue problem:

$$\boldsymbol{M}(\tau)\boldsymbol{w} = \varepsilon\,\boldsymbol{M}_0\boldsymbol{w}. \tag{4.11b}$$

The maximum growth $G(\tau)$ corresponds to the largest eigenvalue of (4.11), i.e.

$$G(\tau) = \varepsilon_{max} \tag{4.12a}$$

while the relevant initial conditions and the forms of disturbances at time τ are given as

$$\boldsymbol{\eta}_{0,max} = \boldsymbol{V}\,\boldsymbol{w}_{max}(\tau), \quad \boldsymbol{\eta}_{max} = \boldsymbol{V}\,\mathrm{e}^{-\mathrm{i}\boldsymbol{\Lambda}\tau}\boldsymbol{V}^{-1}\boldsymbol{\eta}_{0,max} \tag{4.12b}$$

where $\boldsymbol{w}_{max}$ is the eigenvector corresponding to ε_{max}. Note the existence of an alternative method for the determination of the growth. This method involves the evaluation of the largest singular value of the matrix $\boldsymbol{F}\,\mathrm{e}^{-\mathrm{i}\boldsymbol{\Lambda}\tau}\boldsymbol{F}^{-1}$, where $\boldsymbol{F}$ denotes the Choleski factor of $\boldsymbol{M}_0$ (Schmid & Henningson 2001). The corresponding initial conditions follow from the relevant right singular vector.

4.2. *Maximum growth at any time*

We wish to determine the maximum possible growth $G(\tau)$ at any time, i.e.

$$G_{max} = \sup_{\tau>0} G(\tau). \tag{4.13}$$

We left-multiply (4.11*b*) by $\boldsymbol{w}^H$ and utilize the normalization condition to get

$$G(\tau) = \boldsymbol{w}_{max}^H \boldsymbol{M}(\tau)\boldsymbol{w}_{max}. \tag{4.14}$$

The extremum of G occurs for $\tau = \tau_{max}$ when $\mathrm{d}G/\mathrm{d}\tau = 0$. The derivative of G at $t = \tau_{max}$ can be arranged into the following form:

$$\frac{\mathrm{d}G}{\mathrm{d}\tau} = \mathrm{i}\,\boldsymbol{w}_{max}^H[\boldsymbol{\Lambda}^H\boldsymbol{M}_0 - \boldsymbol{M}_0\boldsymbol{\Lambda}]\boldsymbol{w}_{max}G_{max} \tag{4.15}$$

and the condition for the extremum can be written as

$$\boldsymbol{w}_{\tau max}^H[\boldsymbol{\Lambda}^H\boldsymbol{M}_0 - \boldsymbol{M}_0\boldsymbol{\Lambda}]\boldsymbol{w}_{\tau max} = 0, \tag{4.16}$$

where $\boldsymbol{w}_{\tau max} = \boldsymbol{w}_{max}(\tau_{max})$. The above relation has to be solved iteratively as both τ_{max} and $\boldsymbol{w}_{\tau max}$ are not known. We select τ, solve (4.11) for G and $\boldsymbol{w}_{max}$, and use (4.16) to check if the selected τ corresponds to τ_{max}. The initial conditions leading to G_{max} and the corresponding solution have the form

$$\boldsymbol{\eta}_{0,\tau max} = \boldsymbol{V}\,\boldsymbol{w}_{\tau max}, \quad \boldsymbol{\eta}_{\tau max} = \boldsymbol{V}\,\mathrm{e}^{-\mathrm{i}\boldsymbol{\Lambda}\tau_{max}}\boldsymbol{V}^{-1}\boldsymbol{\eta}_{0,\tau max}. \tag{4.17}$$

4.3. *Optimal disturbance and optimal corrugation*

The above analysis has been focused on a particular disturbance characterized by its wavenumbers β and δ assuming that the flow conditions (Re) and the geometry of the corrugation (S, α) are fixed. We now wish to compare all possible disturbances and find the one that gives the largest possible growth at any time, i.e. the largest G_{max}. Such growth is referred to, in the case of a smooth channel, as the optimal growth G_{opt} and the corresponding initial disturbance is called the optimal disturbance and is characterized by the optimal wavenumbers β_{opt} and δ_{opt} (Schmid & Henningson 2001). This problem needs to be generalized in the present case as the largest growth depends on the corrugation geometry. We define the optimal growth as the largest possible growth for any (α, β, δ). The optimal corrugation wavenumber α_{opt} defines the corrugation that is most effective in promoting transient growth (for a given amplitude S) and β_{opt} and δ_{opt} are the optimal wavenumbers defining the optimal disturbance. The time required to reach the optimal growth is referred to as the optimal time τ_{opt}. Note that, since this analysis deals with a limited class of corrugation shapes, the optimal corrugation found here may be sub-optimal as other shapes could result in a larger disturbance growth. Results available in the case of an asymptotic instability (Floryan 2004) show that the analysis with the corrugation shape replaced by its dominant Fourier mode does provide a good estimate of the

$K_V = K_\theta$	G_{max}	τ_{max}
60	249.285	100.061
70	249.248	100.038
80	249.212	100.036

TABLE 1. The effect of the number of Chebyshev polynomials $K_V = K_\theta$ used in the numerical evaluation of G_{max} and τ_{max}. Calculations have been carried out for $S = 0.02$, $\alpha = 3$, $\beta = 2$, $\delta = 0$, $Re = 1000$ using 80 polynomials and 20 Fourier modes for the determination of the basic state, and $M = 8$ Fourier modes and $N = 500$ eigenfunctions/eigenvalues used in the decomposition (4.6) in the transient growth calculations. The numerical parameter selected for the basic state representation effectively reduced the error to a level that is significantly lower that the error associated with the transient growth calculation.

N	G_{max}	τ_{max}
100	248.726	100.053
200	249.019	100.041
300	249.108	100.039
400	249.187	100.038
500	249.248	100.038

TABLE 2. The effect of the number of eigenfunctions/eigenvalues N used in the numerical evaluation of G_{max} and τ_{max}. Calculation have been carried out for $K_V = K_\theta = 70$. All other conditions as in table 1.

M	G_{max}	τ_{max}
6	249.275	100.039
7	249.430	100.051
8	249.248	100.038
9	249.210	100.036

TABLE 3. The effect of the number of Fourier modes M used in the numerical evaluation of G_{max} and τ_{max} calculations have been carried out for $K_V = K_\theta = 70$ and $N = 500$ eigenfunctions/eigenvalues. All other conditions as in table 1.

critical stability parameters and thus the potentially sub-optimal corrugation found here may provide a good estimate of the optimal corrugation.

The complete problem considered here can be posed as finding

$$G_{opt} = \sup_{\beta,\delta,\alpha} G_{max} \tag{4.18}$$

with the corresponding initial disturbance being

$$\boldsymbol{\eta}_{0,opt} = \boldsymbol{\eta}_{0,\tau max}(\beta_{opt}, \delta_{opt}, \alpha_{opt}). \tag{4.19}$$

G_{opt}, $\boldsymbol{\eta}_{0,opt}$ and τ_{opt} are function of both Re and S.

4.4. *Numerical accuracy*

There are several numerical parameters that may affect the accuracy of the solution, e.g. the number of Chebyshev polynomials and the number of Fourier modes used to determine the basic state, the number of Chebyshev polynomials K_v and K_θ and the number of Fourier modes M used to discretize the stability equations, and the number of eigenfunctions/eigenvalues N used in the solution of the transient problem. Tables 1–3 illustrate results of convergence studies and show the correct

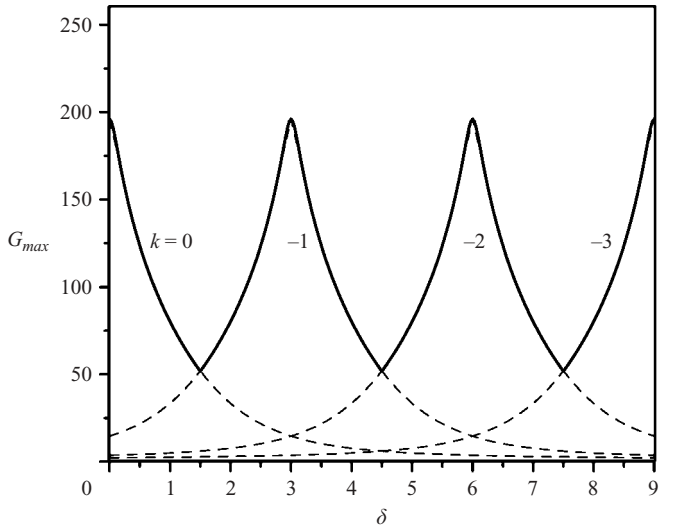

FIGURE 2. Variations of the maximum disturbance growth G_{max} in a smooth channel for the flow Reynolds number $Re = 1000$ and the spanwise disturbance wavenumber $\beta = 2$ as a function of the streamwise disturbance wavenumber δ. Dashed line – classical formulation for an individual subspace characterized by a single value of $\delta \pm k\alpha$, $\alpha = 3$, $k \in (-\infty, +\infty)$; solid line – formulation for a system of subspaces characterized by an infinite set of streamwise wavenumbers $\delta \pm k\alpha$, $\alpha = 3$, $k \in (-\infty, +\infty)$.

values of numerical parameters that guarantee three-digit accuracy. The basic state in this particular test was determined using 20 Fourier modes and 80 Chebyshev polynomials, which guaranteed enforcement of boundary conditions with accuracy $O(10^{-12})$ and reduced the error of determination of the basic state-several orders of magnitude below the error of transient calculations.

5. Discussion of results

The main issue that motivates this analysis is the question of whether surface corrugation increases transient growth compared to the case of smooth channel and, if the answer is affirmative, by how much. We begin the discussion by describing the differences between the properties of the problem in the case of smooth and corrugated channels.

The classical formulation of the transient growth problem in a smooth channel (Schmid & Henningson, 2001) involves disturbances belonging to a single subspace characterized by a pair of streamwise and spanwise wavenumbers (δ, β) and it occurs because of the non-orthogonality of the relevant eigenfunctions. One can construct a number of such subspaces for the streamwise wavenumbers $\delta + k\alpha$, $k = \ldots, -1, 0, 1, \ldots$ with each disturbance set propagating independently from the rest. The maximum growth for each set is illustrated in figure 2 using dashed lines. We can pose another problem where we consider all such (independent) sets together and determine the maximum growth for the whole system. This growth is given by the envelope of growths of individual sets and has periodic form with periodicity α in the δ-direction, as illustrated in figure 2 using solid lines. A formulation involving several disturbance sets is necessary for the corrugated channel where all sets are coupled together. The reader should be aware of the differences between the two

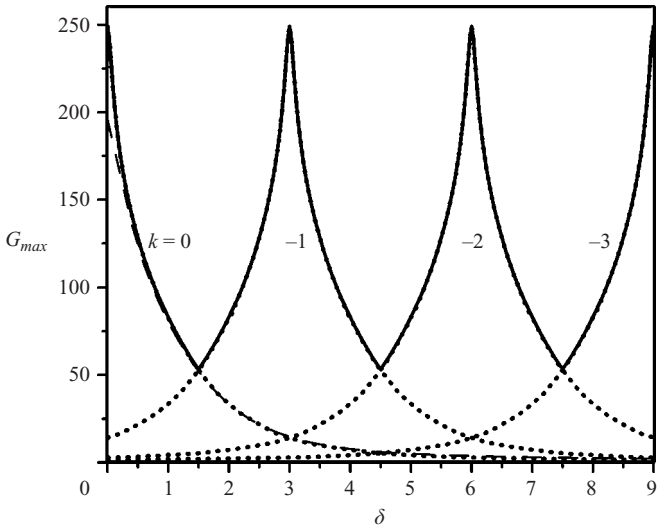

FIGURE 3. Variations of the maximum disturbance growth G_{max} for the flow Reynolds number $Re=1000$ and the spanwise disturbance wavenumber $\beta=2$ as a function of the streamwise disturbance wavenumber δ. Solid line illustrates G_{max} for the corrugated channel with the corrugation amplitude $S=0.02$ and the corrugation wavenumber $\alpha=3$, dotted lines illustrate G_{max} computed for subspaces characterized by $\delta \pm k\alpha$, $\alpha=3$, $k \in (-\infty, +\infty)$ for the same channel, dashed line illustrates G_{max} computed for a smooth channel using classical formulation.

formulations when comparing results for the transient growth in a smooth channel found in the literature (in the classical formulation) and the transient growth in a corrugated channel discussed in this paper.

Disturbance sets $(\beta, \delta + k\alpha)$, $k = \ldots, -1, 0, 1, \ldots$, are coupled together in a corrugated channel, where α is the corrugation wavenumber, and grow as a single entity. The maximum growth is illustrated in figure 3 using solid lines for the same flow conditions as used in figure 2. This growth occurs due to two effects: (i) the non-orthogonality of the eigenfunctions within each subset $(\beta, \delta + k\alpha)$, $k = \ldots, -1, 0, 1, \ldots$, and (ii) the non-orthogonality of the eigenfunctions between the subsets. The former effect (i) is similar to that occurring in smooth channels but its strength is changed due to the corrugation-induced changes of the relevant eigenfunctions. The latter effect (ii) is new. Dotted lines in figure 3 illustrate the growth computed for each subset separately (with interactions between them turned off). The negligible difference between the solid and dotted lines shows that the total growth is dominated by the non-orthogonality effects within each subset for the range of corrugation amplitudes subject to this investigation. The dashed line shown in the same figure illustrates transient growth in a smooth channel using the classical formulation. The difference between the solid and dashed lines shows that the maximum transient growth increases by about 25% due to the presence of the corrugation for the flow conditions used in this example and is concentrated around $\delta \approx 0$ and negligible elsewhere (the large difference for the larger values of δ is due to the periodic character of G_{max} in the corrugated channel and should be omitted from this comparison). Note that $\delta = k\alpha$, $k = \ldots, -1, 0, 1, \ldots$, correspond to streamwise vortices (that are modulated by the corrugation).

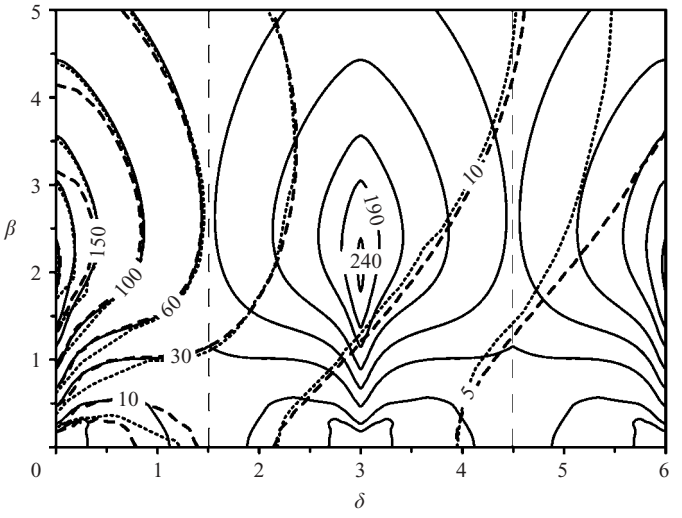

FIGURE 4. Variations of the maximum disturbance growth G_{max} as a function of the disturbance wavenumbers β and δ for the flow Reynolds number $Re = 1000$. Solid lines illustrate G_{max} for the complete problem for the corrugation wavenumber $\alpha = 3$ and the corrugation amplitude $S = 0.02$, dotted lines illustrate G_{max} computed for a single subspace characterized by the wavenumber δ for the same channel and dashed lines illustrate G_{max} for a smooth channel in the classical formulation.

Variations of the maximum growth as a function of the disturbance wavenumbers β and δ for the fixed corrugation geometry ($S = 0.01$, $\alpha = 3$) are illustrated in figure 4 for $Re = 1000$. The same figure shows the growth computed for a single subset characterized by the wavenumber δ and for the smooth channel using the classical formulation. It can be seen that the total, subset and smooth channel growths are very similar when $\delta < \alpha/2$ except for $\delta \approx 0$ and $\beta \approx 2$–3 where large differences occur. It appears that corrugation increases the growth of disturbances that are approximately optimal in the case of a smooth channel, and has little effects on the growth in the other cases. The large difference between the growth for the complete problem and the subset and smooth channel growths for $\delta > \alpha/2$ occur due to different functional spaces used in each case and is irrelevant for the comparison with the growth in a smooth channel.

Variations of G_{max} when the corrugation wavenumber varies from $\alpha = 1$ to $\alpha = 10$ for the fixed corrugation amplitude $S = 0.01$ at a fixed Reynolds number $Re = 1000$ are illustrated in figure 5. The growth is periodic with respect to δ/α and thus the plots are limited to the range $\delta/\alpha \in (-0.5, 0.5)$. It can be seen that the optimal growth occurs at $\delta = 0$, $\beta \approx 2$ and it takes the value of $G_{opt} = 199, 206, 203$ for $\alpha = 1, 3, 10$, respectively, i.e. it is rather insensitive to variations of α in the range of α studied. Note that G_{opt} decreases when α increases from 3 to 10, which suggests that further increase of α would not result in an increased G_{opt}. The same figure gives results for the smooth channel. It can be seen that the presence of the corrugation has a very small effect on the transient growth compared with the smooth channel at such small values of Re and S (the optimal growth for the smooth channel is $G_{opt} = 196$).

Variations of G_{max} when the flow Reynolds number increases from $Re = 1000$ to $Re = 3000$ for the fixed corrugation geometry ($\alpha = 3$, $S = 0.01$) are illustrated in figure 6. The optimal growth G_{opt} occurs at $\delta = 0$, $\beta \approx 2$ and rapidly increases with

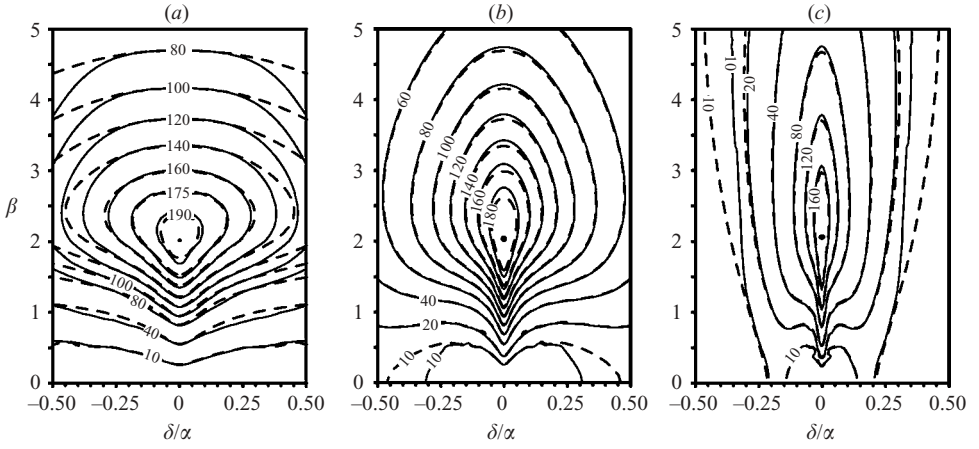

FIGURE 5. Variations of the maximum disturbance growth G_{max} as a function of the corrugation wavenumber α for the flow Reynolds number $Re = 1000$ and the corrugation amplitude $S = 0.01$. $\alpha = 1$, 3, 10 in (a), (b) and (c), respectively. Dashed lines illustrate G_{max} for the smooth channel in the classical formulation. The optimal value of the disturbance growth is $G_{opt} = 196$, 199, 206, 203 for the smooth channel and the corrugated channel with $\alpha = 1$, 3, 10, respectively.

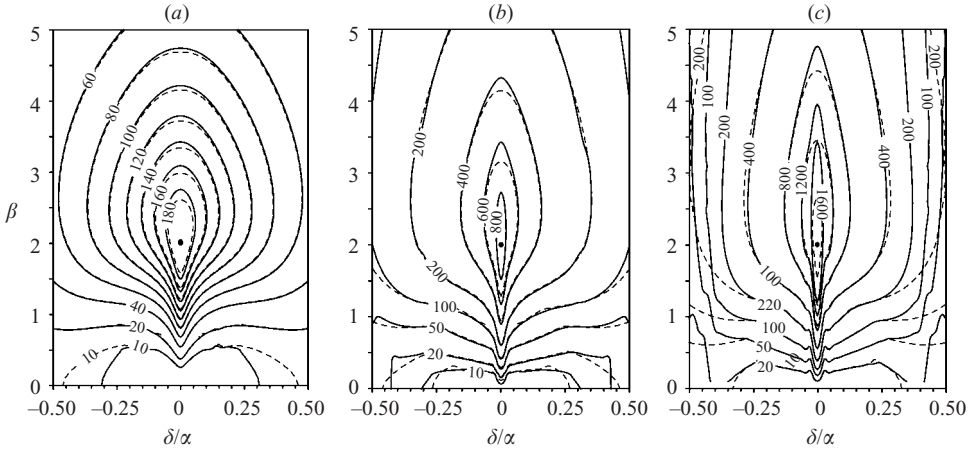

FIGURE 6. Variations of the maximum disturbance growth G_{max} as a function of the flow Reynolds number for a corrugated wall with the corrugation wavenumber $\alpha = 3$ and the corrugation amplitude $S = 0.01$. $Re = 1000$, 2000, 3000 in (a), (b) and (c), respectively. Dashed lines illustrate G_{max} for the smooth channel in the classical formulation. The optimal value of the disturbance growth in the corrugated channel is $G_{opt} = 206$, 922, ∞ (asymptotic instability) for $Re = 1000$, 2000, 3000, respectively, while it is 196, 784, 1763 for the smooth channel.

Re, i.e. it is 206 (196), 922 (784) and ∞ (1763) for $Re = 1000$, 2000, 3000, respectively, where values in the brackets correspond to the smooth channel. Note that the flow is asymptotically unstable at $Re = 3000$. The same figure gives results for a smooth channel; comparison of the results shows that corrugation represents an effective amplifier for the optimal disturbances, but its effect on other disturbances can be considered negligible.

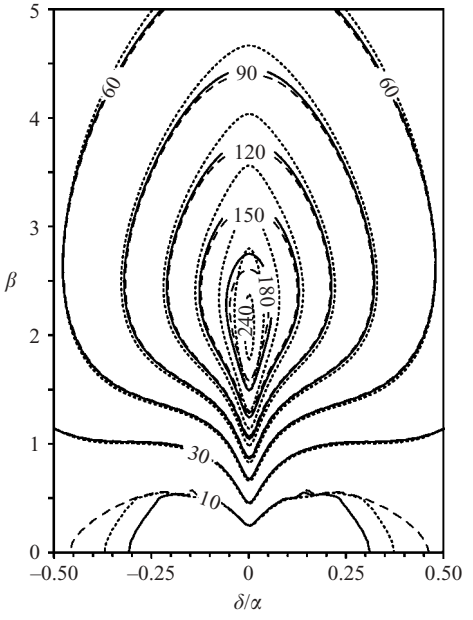

FIGURE 7. Variations of the maximum disturbance growth G_{max} as a function of the corrugation amplitude for the corrugation wavenumber $\alpha = 3$ and the flow Reynolds number $Re = 1000$. Dotted, solid and dashed lines correspond to the corrugation amplitude $S = 0.02$, 0.01, 0, respectively. Classical formulation is used in the case of smooth channel ($S = 0$). The optimal value of the disturbance growth is $G_{opt} = 196, 206, 250$ for $S = 0, 0.01, 0.02$, respectively.

Variations of G_{max} when the corrugation amplitude increases from $S = 0$ to $S = 0.02$ for $Re = 1000$ and $\alpha = 3$ are illustrated in figure 7. The optimal growth remains at $\delta = 0$, $\beta \approx 2$ and takes values $G_{opt} = 197$, 206, 250 for $S = 0$, 0.01, 0.02, respectively. The largest increase of G_{max} as a function of S occurs for the optimal disturbances and can be considered insignificant for other disturbances in the range of parameters studied.

Dependence of the optimal growth G_{opt}, the optimal corrugation wavenumber α_{opt} and the optimal time τ_{opt} on the corrugation amplitude S and the flow Reynolds number Re is illustrated in figures 8, 9 and 10, respectively. The optimal conditions always occur for the streamwise disturbance wavenumber $\delta_{opt} = k\alpha$, $k = \ldots, -1, 0, 1, \ldots$, while the optimal spanwise disturbance wavenumber β_{opt} changes in the narrow interval $\beta_{opt} \in (2.04, 2.1)$ in the range of parameters studied. It can be seen that α_{opt} decreases from 4.4 to 3 when S increases from 0.005 to 0.02 (figure 9), i.e. corrugations with longer wavelength are more effective in increasing transient growth when the corrugation amplitude increases. The optimal growth G_{opt} is fairly insensitive to the increase of S as long as Re is below its critical value Re_{cr} (for the maximum S considered) that gives rise to the vortex instability similar to that described by Floryan (2003) (see figure 8). G_{opt} increases approximately proportionally to Re^2 for $Re < Re_{cr}$ similarly to the smooth channel case (Trefethen *et al.* 1993), but this growth rapidly accelerates for $Re > Re_{cr}$ and S sufficiently high (figure 8). The same observation applies to τ_{opt} (see figure 10).

We shall now focus our attention on the form of optimal disturbances. Figure 11 displays the distribution of the (y, z)-component (v_D, w_D) of the initial ($t = 0$) optimal disturbance velocity vector for $z \in (0, 2\pi/\beta)$, $Re = 1000$, $\beta = 2$, $\delta = 0$, $\alpha = 3$, $S = 0.02$ at

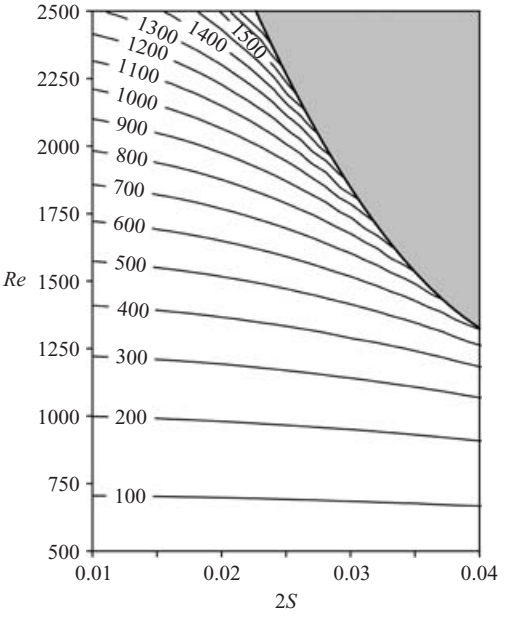

FIGURE 8. Variations of the optimal growth G_{opt} as a function of the corrugation amplitude S and the flow Reynolds number Re. G_{opt} occurs for $\delta = 0$ and β in the narrow interval (2.04, 2.1). Grey area denotes conditions for the occurrence of modal instability of the type discussed by Floryan (2003).

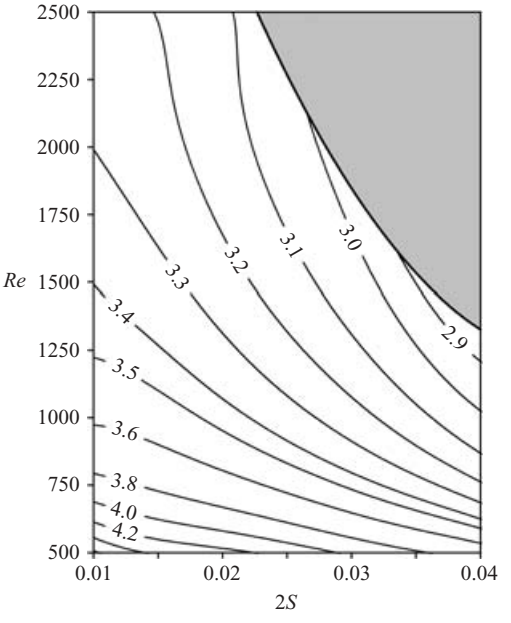

FIGURE 9. Variations of the optimal corrugation wavenumber α_{opt} corresponding to the optimal growth G_{opt} shown in figure 8 as a function of the corrugation amplitude S and the flow Reynolds number Re. α_{opt} occurs for $\delta = 0$ and β in the narrow interval (2.04, 2.1). Grey area denotes conditions for the occurrence of modal instability of the type discussed by Floryan (2003).

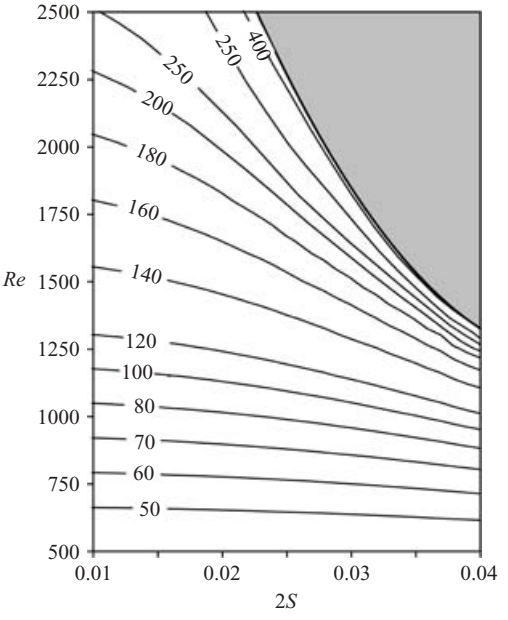

FIGURE 10. Variations of the optimal time τ_{opt} corresponding to the optimal growth G_{opt} shown in figure 8 as a function of the corrugation amplitude S and the flow Reynolds number Re. τ_{opt} occurs for $\delta = 0$ and β in the narrow interval (2.04, 2.1). Grey area denotes conditions for the occurrence of modal instability of the type discussed by Floryan (2003).

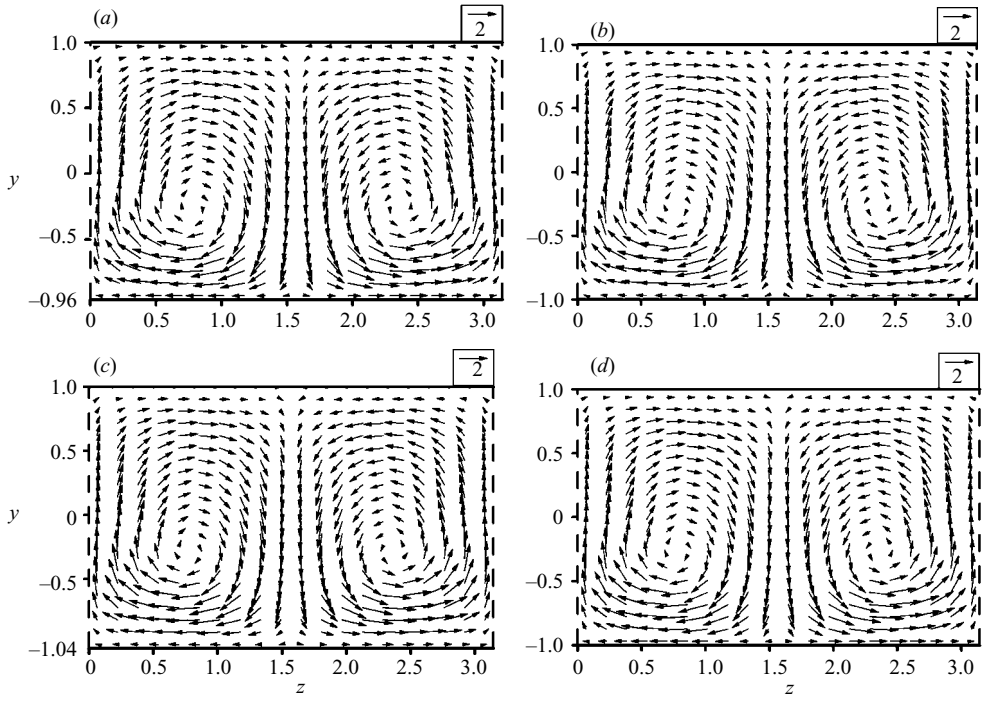

FIGURE 11. Distribution of the (y, z)-component of the optimal disturbance velocity vector for $z \in (0, 2\pi/\beta)$, $Re = 1000$, $\beta = 2$, $\delta = 0$, $\alpha = 3$, $S = 0.02$ at the initial time $t = 0$. (*a*) $x = 0$, (*b*) $x = \lambda_x/4$, (*c*) $x = \lambda_x/2$, (*d*) $x = 3\lambda_x/4$ where $\lambda_x = 2\pi/\alpha$ denotes wavelength of the corrugation. Scale for the vector magnitude is shown above each figure.

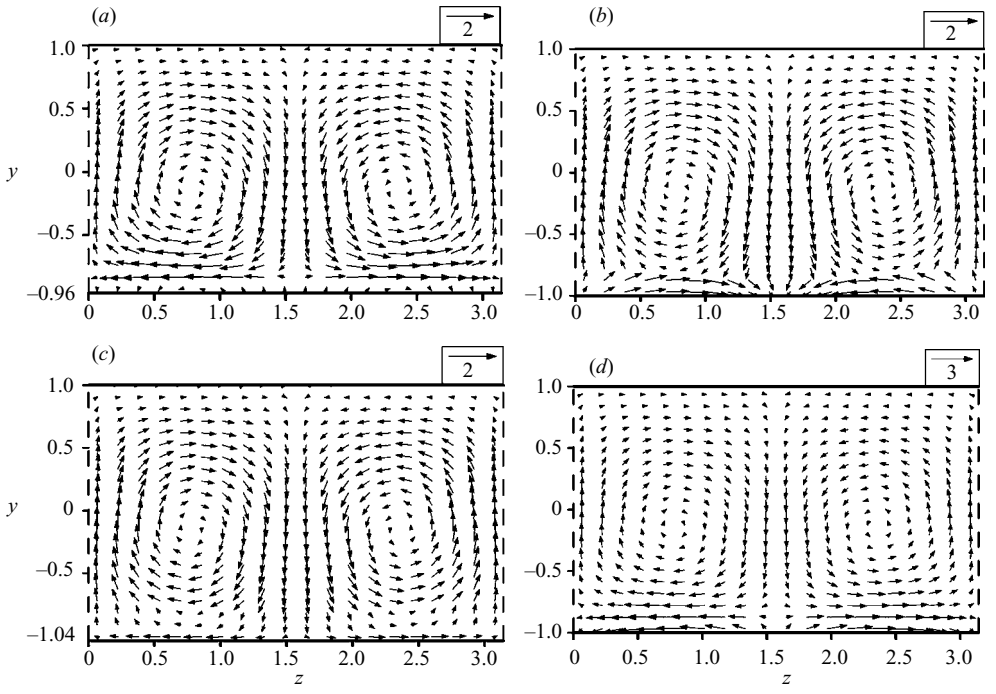

FIGURE 12. Distribution of the (y, z)-component of the optimal disturbance velocity vector at the optimal time $\tau_{opt} = 100$. The remaining conditions as in figure 11. (*a*) $x = 0$, (*b*) $x = \lambda_x/4$, (*c*) $x = \lambda_x/2$, (*d*) $x = 3\lambda_x/4$.

four locations along the streamwise direction at $x = 0$, $\lambda_x/4$, $\lambda_x/2$, and $3\lambda_x/4$, where $\lambda_x = 2\pi/\alpha$ stands for the wavelength of the corrugation. All results are normalized with condition $E_k(0) = 1$ unless otherwise noted. The initial disturbance has the form of pairs of streamwise vortices that are slightly modulated along the x-direction; the maximum magnitude of the velocity vector in this plane at all x-cross-sections is about 10. Figure 12 shows the same component of the disturbance velocity vector, but at time $t = \tau_{opt}$. Strong modulation in the x-direction is clearly visible with the vortical motion slowing down on the downhill side of the corrugation peak (figure 12*b*, *c*) and accelerating on the uphill side (figure 12*a*, *d*). The motion is concentrated closed to the corrugated wall on the uphill side (figure 12*d*, the maximum magnitude of velocity vector is around 10 here). It diffuses towards the centre of the channel at the peak of the corrugation (figure 12*a*). It slows down on the downhill side (figure 12*b*, the maximum size of the velocity vector is about 5 here) where the motion in the opposite direction develops next to the corrugated wall. The reversed motion is clearly visible in figure 13 displaying an enlargement of the bottom part of figure 12(*b*). The vortex begins its recovery at the valley location (figure 12*c*) where the counter-motion disappears and rapidly accelerates on the uphill side (figure 12*d*). Comparison of figures 11 and 12 shows a slight slowdown and significant redistribution of the vortex motion between the initial and optimal times.

We shall now consider changes in the streamwise component u_D of the disturbance velocity vector. Figure 14 displays u_D associated with the optimal disturbance at time $t = 0$ for the same conditions as the v_D, w_D components discussed above and with the same normalization. u_D has a rather complex distribution with a slight streamwise modulation associated with the presence of the corrugation at the initial time $t = 0$;

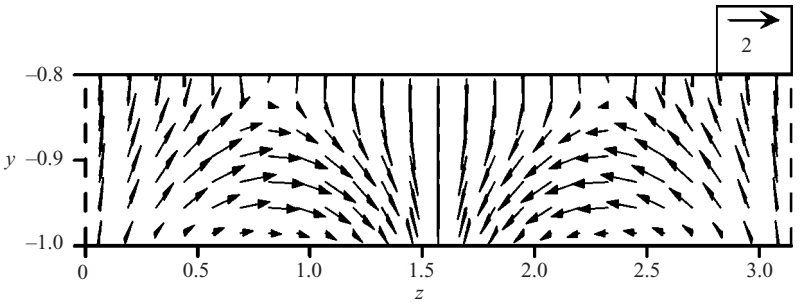

FIGURE 13. Enlargement of the segment of the (y, z)-component of the optimal disturbance velocity vector near the lower wall at $x = \lambda_x/4$ at the optimal time $\tau_{opt} = 100$. The remaining conditions as in figure 11.

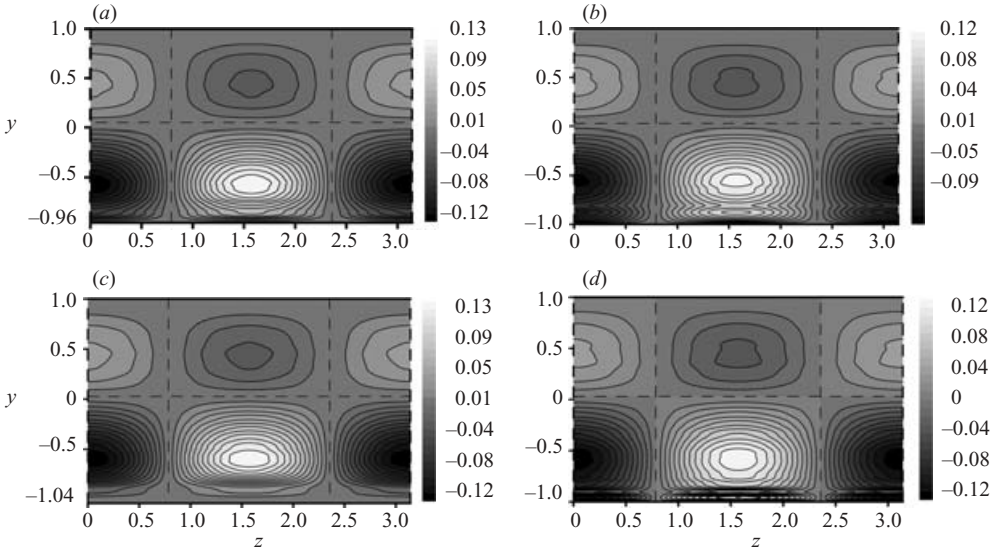

FIGURE 14. Distribution of the x-component u_D of the disturbance velocity vector at the initial time $t = 0$. The remaining conditions as in figure 11. (*a*) $x = 0$, (*b*) $x = \lambda_x/4$, (*c*) $x = \lambda_x/2$, (*d*) $x = 3\lambda_x/4$. Dashed lines identify zero value.

its values change between -1 and $+1$ as dictated by the normalization (see figure 14). The magnitude of u_D grows significantly as time increases and reaches values in the range of approximately -300 to 300 at the optimal time $t = \tau_{opt}$ (see figure 15). This acceleration is associated with the lift-up effect that leads to the formation of streaks. The distribution of u_D becomes well-organized at the optimal time, even at the downstream side of the corrugation peak where vortex motion changes direction, as illustrated in figure 16 displaying enlargement of the bottom of figure 15(*b*). There is an significant modulation of u_D in the streamwise direction, especially in the section between $x = \lambda_x/4$ (figure 15*b*) and $x = \lambda_x/2$ (figure 15*c*).

The formation of the streak is illustrated in figure 17 that displays the (x, y) component of the optimal disturbance velocity vector. The motion is primarily in the y-direction and has the magnitude $O(10)$ at the initial time $t = 0$, as illustrated in figure 17(*a*). It is re-directed into the x-direction and reaches values $O(300)$ at the optimal time $t = \tau_{opt}$, as shown in figure 17(*b*).

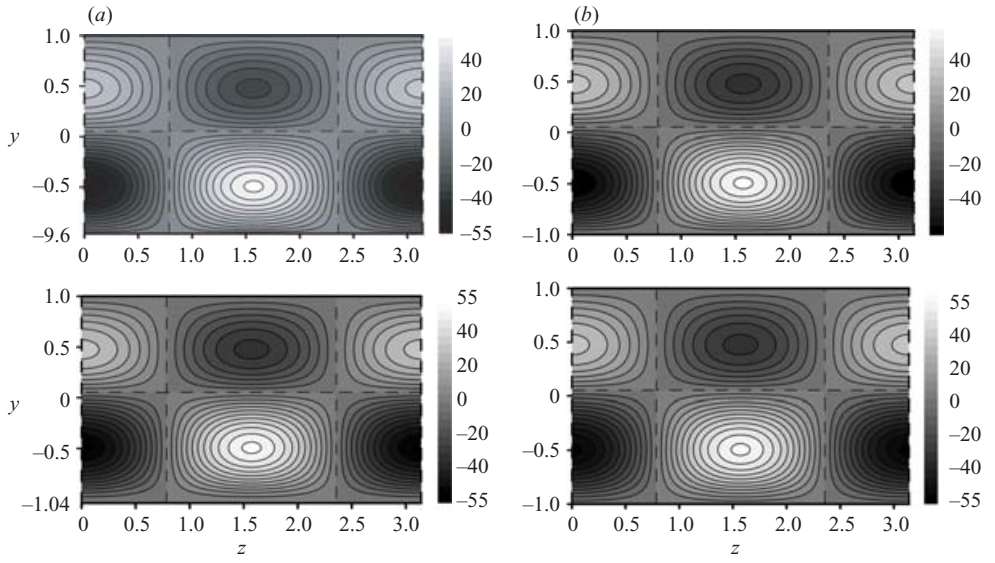

FIGURE 15. Distribution of the x-component u_D of the disturbance velocity vector at the optimal time $\tau_{opt} = 100.05$. The remaining conditions as in figure 11. (*a*) $x = 0$, (*b*) $x = \lambda_x/4$, (*c*) $x = \lambda_x/2$, (*d*) $x = 3\lambda_x/4$. Dashed lines identify zero value.

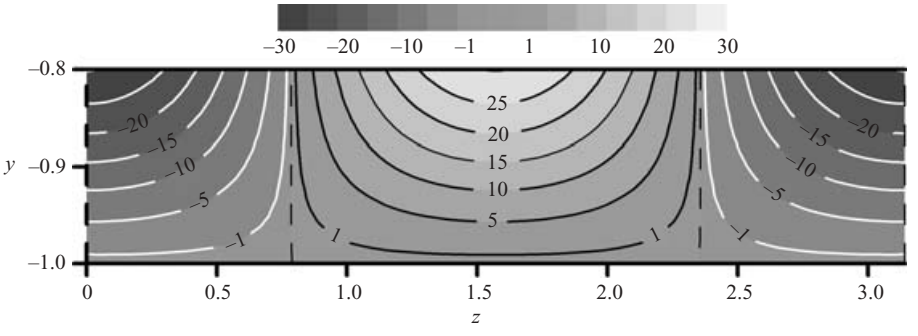

FIGURE 16. Enlargement of the segment of the x-component u_D of the optimal disturbance velocity vector near the lower wall at $x = \lambda_x/4$ at the optimal time $\tau_{opt} = 100$. The remaining conditions as in figure 11.

The above discussion shows that the presence of the corrugation increases the magnitude of the transient growth, compared with the smooth channel case, but this increase is not very dramatic and thus cannot by itself explain the rapid transition observed in flows over rough walls (Corke *et al.* 1986). Also, the optimal disturbances are qualitatively similar in both cases, i.e. they have the form of streamwise vortices that lead to the formation of streamwise streaks. The possible explanation of the role of the corrugation in accelerating the transition process may be found by looking at the details of the disturbance motion and, especially, at the differences in the form of the transverse shear layers being set up by the optimal disturbances in both cases. We shall now discuss this issue.

Transverse motion has already been discussed in the context of the description of vortical motion in the (y, z)-plane (figures 11–13). We now provide more details. Figure 18 displays the distribution of the spanwise component w_D of the optimal

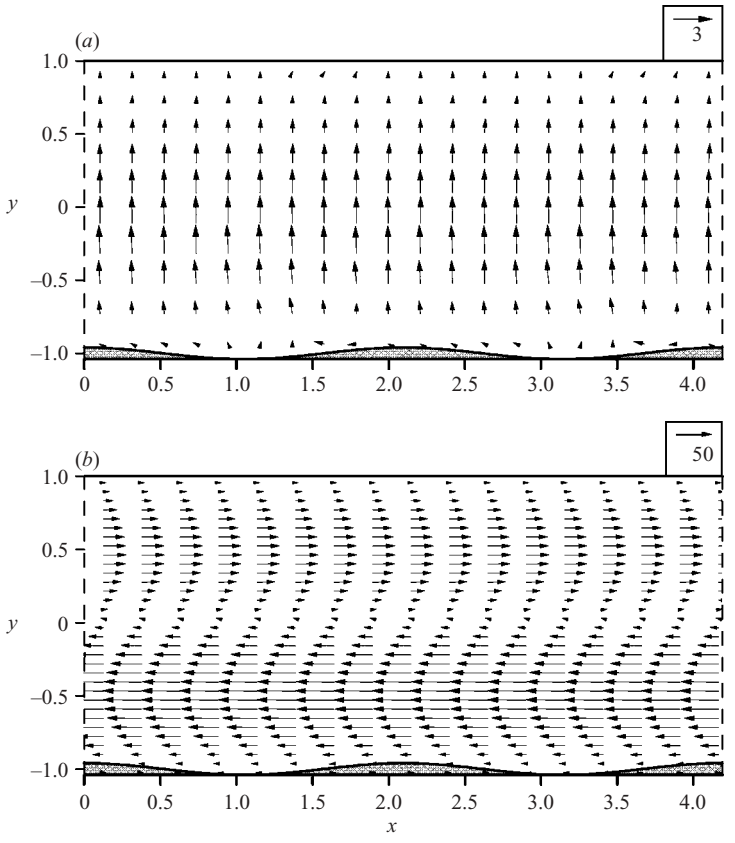

FIGURE 17. Distribution of the (x, y)-component of the disturbance velocity vector at $z = 0$. The remaining conditions as in figure 11. (*a*) $t = 0$, (*b*) $t = \tau_{opt} = 100$.

disturbance vector in the (x, y)-plane. A weak streamwise modulation can be observed at the initial time $t = 0$ (figure 18*a*) but very strong modulation can be seen at the optimal time $t = \tau_{opt}$ (figure 18*b*). This modulation results in the change of direction of the vortical motion on the downstream side of the corrugation peak and thus leads to the formation of strong transverse shear layers that may be subject to dynamic instabilities. The form of spanwise shears layers is displayed in figure 19 at four streamwise locations $x = 0$, $\lambda_x/4$, $\lambda_x/2$, $3\lambda_x/4$ with figures 19(*a*) and 19(*b*) showing data at the initial time $t = 0$ and the optimal time $t = \tau_{opt}$, respectively. The same figure shows equivalent data for the smooth wall. Significantly stronger shear layers exist in the case of the corrugated wall at $t = \tau_{opt}$ and dynamic instabilities of these layers are most likely to accelerate the transition process in the case of corrugated walls. Figure 20 displays distributions of the streamwise component u_D of the optimal disturbance velocity vector for the same conditions. There is a significant streamwise modulation in the case of a corrugated wall, with the formation of inflectional velocity profiles (note a significant scale difference between figures 20*a* and 20*b*).

Results discussed above have been obtained for the optimal corrugation of $\alpha = 3$. Such a corrugation has a fairly long wavelength that one typically does not associate with surface roughness. Figures 21 and 22 display the form of shear layers discussed above but for the corrugation wavenumber $\alpha = 15$ (this is not an optimal corrugation for these conditions). Note that the streamwise modulation is limited to a very thin

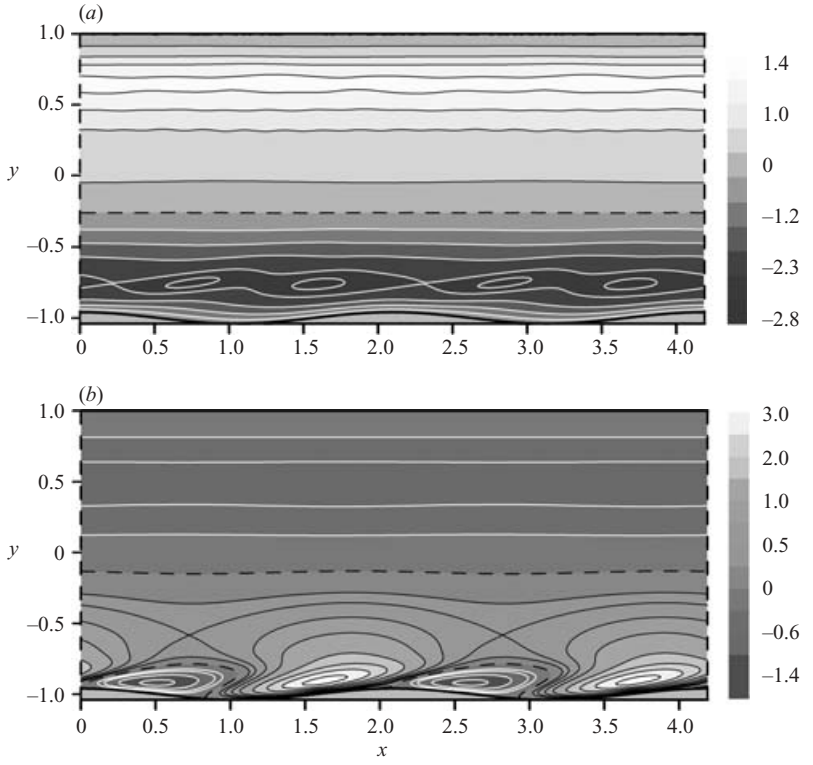

FIGURE 18. Distribution of the z-component w_D of the disturbance velocity vector at $z = \lambda_z/4$ where $\lambda_z = 2\pi/\beta$ denotes spanwise wavelength of the disturbance field. (a) $t = 0$, (b) $t = \tau_{opt} = 100$. The remaining conditions as in figure 11. Black and white lines denote positive and negative quantities, respective; dashed line corresponds to zero value.

layer next to the corrugated wall (see figure 21b) with the rest of the profile being marginally affected by the corrugation. The dynamic instabilities are most likely weaker and, as the current analysis shows, the transient growth is smaller for such corrugation. While the shorter corrugation appears to be less effective in promoting disturbance growth, it should not be dismissed as the transient growth is not much smaller and the issue of dynamics instabilities needs to be thoroughly analysed before drawing final conclusions.

The final comment that we make here is to point out the rather complex form of the optimal disturbances (see figures 20a and 22a). It is unlikely that such disturbances can occur naturally and thus the fate of the flow system will probably be dictated by the dynamics of sub-optimal disturbances.

We now focus our attention on the interplay between the asymptotic (modal) instability and the transient growth. Figure 23 illustrates transient growth as a function of time for $Re = 2000$, $\beta = 2$, $\delta = 0$, $\alpha = 3$ for different corrugation amplitudes S. In each case the initial conditions have been selected to maximize the growth at time $t = 50$. Note a very rapid initial growth regardless of the values of S. This growth eventually either disappears and disturbances decay for subcritical values of S or asymptotic growth takes over and disturbances grow without limits for the supercritical values of S. Asymptotic growth leads to the vortex instability of the type discussed by Floryan (2003). Onset of transition requires activation of nonlinear effects, which will certainly

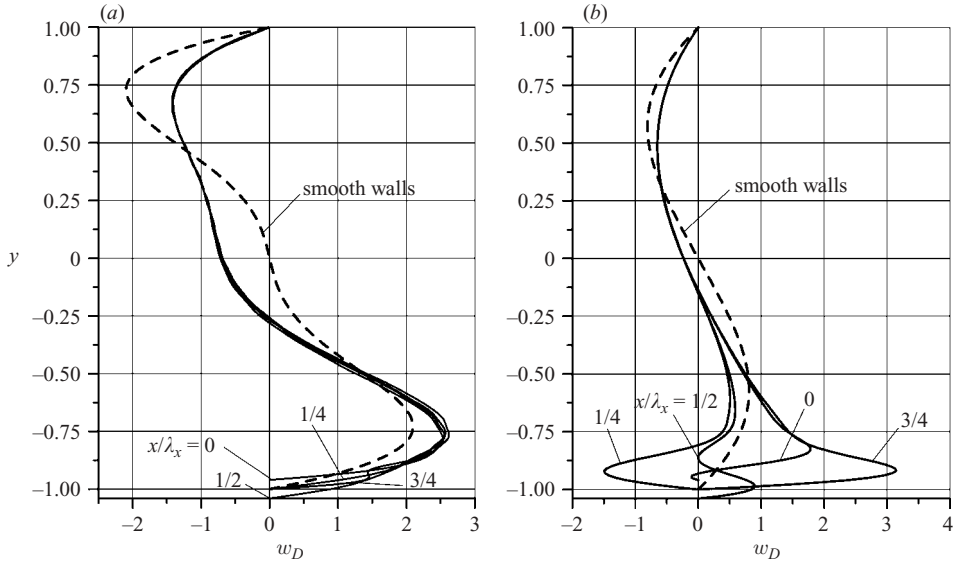

FIGURE 19. Distribution of the spanwise optimal disturbance velocity component w_D across the channel at four streamwise locations $x = 0$, $\lambda_x/4$, $\lambda_x/2$, $3\lambda_x/4$, for $Re = 1000$, $\beta = 2$, $\delta = 0$, $\alpha = 3$, $S = 0.01$. (*a*) $t = 0$, (*b*) $t = \tau_{opt} = 80$. Dashed lines give results for the optimal disturbance in the case of smooth walls at the initial time $t = 0$ and at the optimal time $t = \tau_{opt} = 76$ for such disturbances.

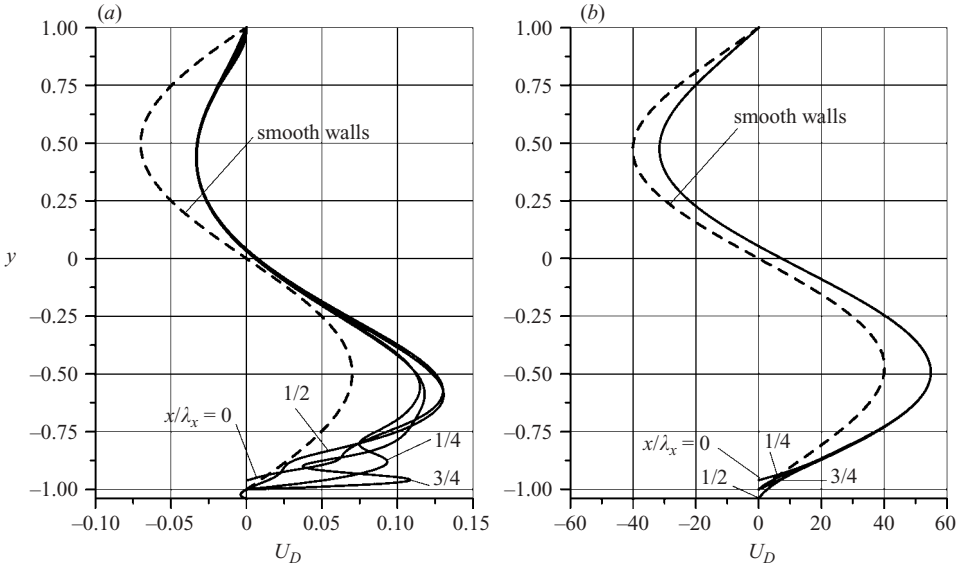

FIGURE 20. Distribution of the streamwise disturbance velocity component u_D across the channel. The remaining conditions as in figure 19. (*a*) $t = 0$, (*b*) $t = \tau_{opt} = 80$.

come into play in the case of modal instability. The transient growth is however much stronger than the modal instability and it may decide the fate of the flow even in the case of supercritical values of S. Results shown in figure 23 demonstrate that the transient growth will amplify disturbances by a factor of 500–1000 before modal instability

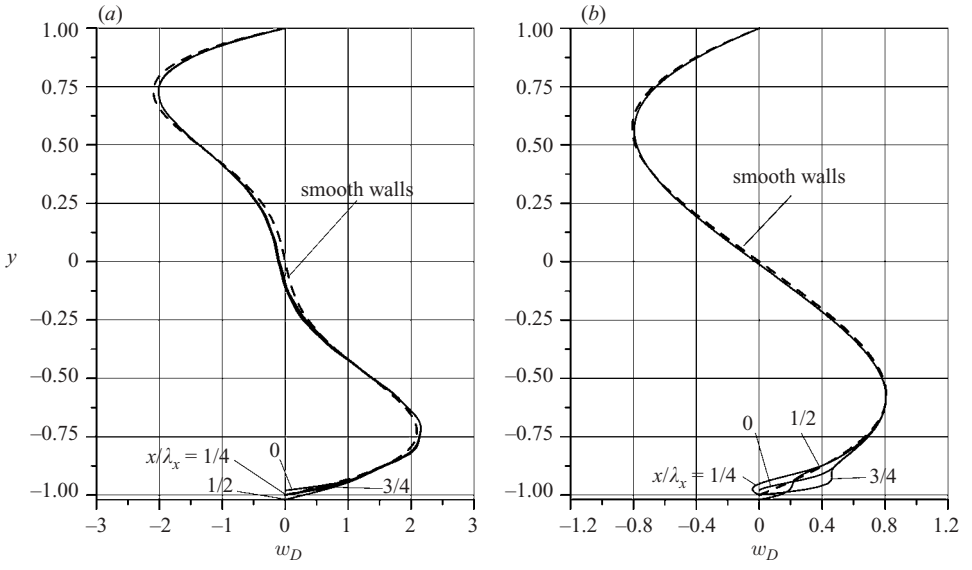

FIGURE 21. Distribution of the spanwise disturbance velocity component w_D across the channel for $\alpha = 15$, $S = 0.01$. The remaining conditions as in figure 19. (*a*) $t = 0$, (*b*) $t = \tau_{opt} = 77$.

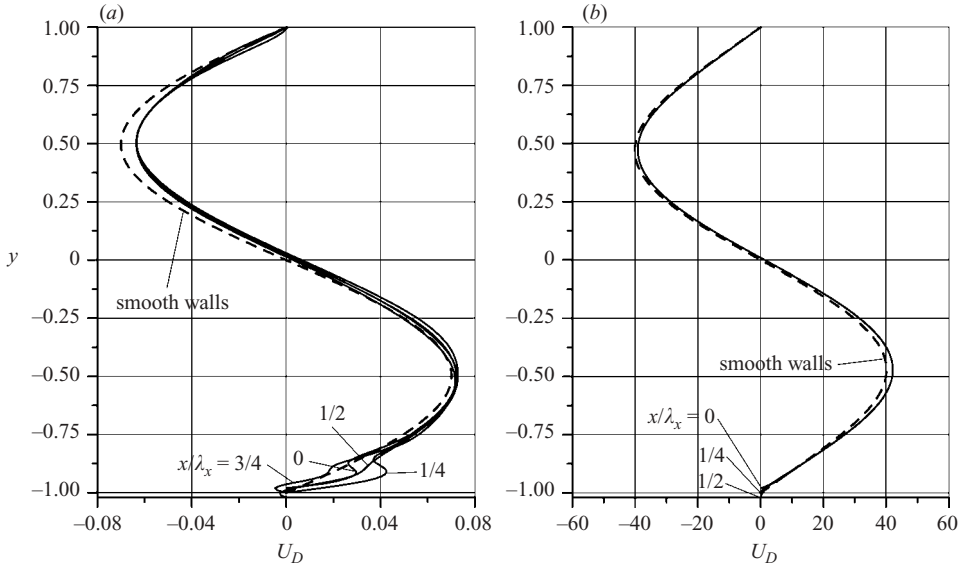

FIGURE 22. Distribution of the streamwise disturbance velocity component u_D across the channel. The remaining conditions as in figure 21. (*a*) $t = 0$, (*b*) $t = \tau_{opt} = 77$.

catches up. These results suggest that when the flow has large levels of background disturbances, the transient growth will most likely dominate the initial stages of the laminar–turbulent transition. If background disturbances are eliminated, the modal instability will have a chance to develop and it will dominate the transition process.

Finally we comment on the use of surface corrugation as a tool for flow control. The effectiveness of corrugation depends on the flow conditions and the corrugation

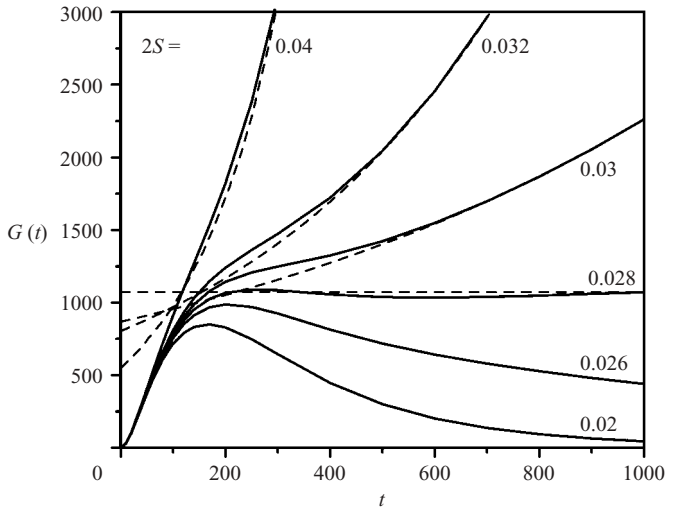

FIGURE 23. Transient growth as a function of time for $Re = 2000$, $\beta = 2$, $\delta = 0$, $\alpha = 3$ for different values of the corrugation amplitude S. Initial conditions are selected in such a manner that the growth G at time $t = 50$ attains maximum for each S. Dashed lines illustrate asymptotes defined by the modal (asymptotic) instability for the supercritical values of S.

geometry. Figure 24 illustrates this as well as the potential of the corrugation for manipulation of transient growth for $Re = 3000$. When $S = 0.008$, the maximum transient growth G_{max} is finite and its maximum is fairly flat in the α-direction, i.e. α in the range from 1.5 to 7.5 gives G_{max} that changes within 10 % of G_{opt} (see figure 24*a*). A very small increase of S, i.e. $\Delta S = 0.002$, significantly increases G_{max} around the optimal conditions and gives rise to modal instability (see figure 24*b*). Increase of S by another 0.002 dramatically expands the range of modal instability (see figure 24*c*). These results demonstrate the dramatic effects of the corrugation amplitude, assuming that it first reaches a certain minimum value. The effects of the corrugation wavenumber are less significant, assuming that α is in the correct range.

6. Summary

We have carried out an analysis of transient growth of disturbances in a rough channel. A general linear transient growth theory has been formulated where the roughness geometry is represented using Fourier expansions. The explicit calculations have been carried out for the case of channel bounded by one rough and one smooth wall with the roughness represented by a single Fourier mode resulting in a sinusoidal (wavy) wall corrugation. The spectrally accurate numerical method that relies on the Chebyshev expansions has been used. The boundary conditions at the rough wall have been enforced using the immersed boundary conditions concept.

The transient growth occurs due to the non-normality of the relevant operator. The operator consists of a system of coupled sub-operators associated with different Fourier modes. The growth may occur due to the non-orthogonality of the eigenfunctions within each sub-operator as well as to the non-orthogonality of the eigenfunctions between sub-operators. It has been found that the former effect is dominant in the range of parameters covered by this investigation.

The surface corrugation appears to increase the growth of disturbances but only those that are approximately optimal in the smooth wall case. The magnitude of this

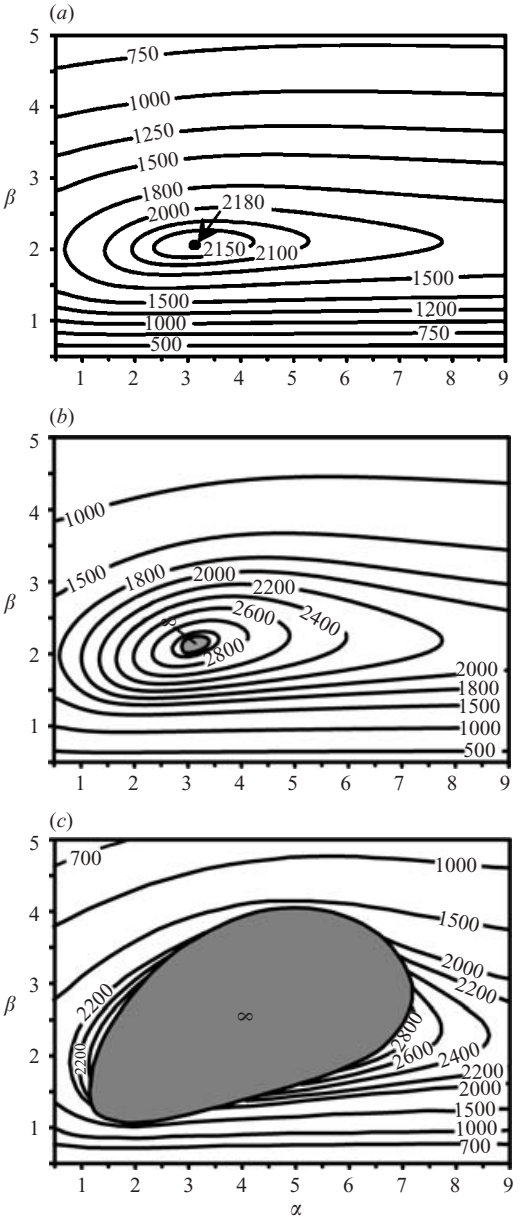

FIGURE 24. Variations of the maximum growth G_{max} as a function of the corrugation wavenumber α and the spanwise disturbance wavenumber β for the flow Reynolds number $Re = 3000$ and the streamwise disturbance wavenumber $\delta = 0$. (*a*) Corrugation amplitude $S = 0.008$, (*b*) $S = 0.010$, (*c*) $S = 0.012$. Grey areas denote conditions for the occurrence of modal instability of the type discussed by Floryan (2003).

additional growth depends on the distance in the parameter space from the conditions giving rise to the modal (asymptotic) instability and can vary from very modest to very large on getting closer to the onset of the instability.

The optimal growth, which is defined as the maximum possible growth for the given corrugation amplitude, has been identified for the corrugation amplitudes $S < 0.02$

and the flow Reynolds numbers $Re < 2500$. The corrugation shape that leads to the optimal growth, i.e. the optimal corrugation, has also been found; the optimal corrugation wavenumber decreases from $\alpha_{opt} = 4.4$ to $\alpha_{opt} = 3$ as the corrugation amplitude increases from $S = 0.005$ to $S = 0.02$. It has been found that the optimal disturbance, i.e. the disturbance that results in the optimal growth, has the form of streamwise vortices with the spanwise wavenumber $\beta_{opt} \in (2.04, 2.1)$ in the range of parameters of this investigation.

Comparison of the temporal growth with the growth associated with the modal (asymptotic) instability shows that the former may reach the values of 500–1000 before the modal instability catches up. This result suggests that the temporal growth mechanism may dominate the transition process in a noisy environment. It is demonstrated that the growth process can be manipulated by changing the geometry of the corrugation.

This work has been carried out with support of SHARCNET and NSERC of Canada. SHARCNET of Canada provided computing resources. The authors would like to thank P. Huang for carrying out part of the computations.

Appendix A

Operators used in equations (3.6) are defined as follows:

$$
\begin{aligned}
G_v^{(m,n)} &= Re\left[\frac{\mathrm{i}\,n\alpha}{k_{m-n}^2}(\beta^2 - \gamma_m\gamma_{m-n})\,\mathrm{D}f_u^{(n)}\,\mathrm{D} + \frac{k_m^2}{k_{m-n}^2}(\beta^2 + \gamma_{m-n}\gamma_{m-2n})\,f_v^{(n)}\,\mathrm{D}\right.\\
&\quad + \frac{\mathrm{i}}{k_{m-n}^2}\left(2n\alpha\beta^2 - \gamma_m k_{m-n}^2\right)f_u^{(n)}\,\mathrm{D}^2 + \frac{\mathrm{i}}{k_{m-n}^2}\left(n\alpha\gamma_m - k_m^2\right)\,f_v^{(n)}\,\mathrm{D}^3\\
&\quad \left.+\mathrm{i}\,k_m^2\gamma_{m-2n}f_u^{(n)} + \mathrm{i}\,\gamma_m\mathrm{D}^2 f_u^{(n)}\right],\\
\hat{G}_v^{(m,n)} &= Re\left[\frac{\mathrm{i}\,n\alpha}{k_{m+n}^2}(\gamma_m\gamma_{m+n} - \beta^2)\left(\mathrm{D}f_u^{(n)}\right)^*\mathrm{D} + \frac{k_m^2}{k_{m+n}^2}(\beta^2 + \gamma_{m+n}\gamma_{m+2n})\left(f_v^{(n)}\right)^*\mathrm{D}\right.\\
&\quad + \frac{\mathrm{i}}{k_{m+n}^2}\left(-2n\alpha\beta^2 - \gamma_m k_{m+n}^2\right)\left(f_u^{(n)}\right)^*\mathrm{D}^2 + \frac{\mathrm{i}}{k_{m+n}^2}\left(-n\alpha\gamma_m - k_m^2\right)\left(f_v^{(n)}\right)^*\mathrm{D}^3\\
&\quad \left.+\mathrm{i}\,k_m^2\gamma_{m+2n}\left(f_u^{(n)}\right)^* + \mathrm{i}\,\gamma_m\left(\mathrm{D}^2 f_u^{(n)}\right)^*\right],\\
G_v^{(0)} &= -\mathrm{i}\gamma_m\left[f_u^{(0)}\left(\mathrm{D}^2 - k_m^{(2)}\right) - \mathrm{D}^2 f_u^{(0)}\right],\\
G_\theta^{(m,n)} &= Re\left[\frac{1}{k_{m-n}^2}2n\alpha\beta\gamma_{m-n}f_u^{(n)}\,\mathrm{D} + \frac{n\alpha\beta}{k_{m-n}^2}(\gamma_m + \gamma_{m-n})\,\mathrm{D}f_u^{(n)}\right.\\
&\quad \left.-\frac{\mathrm{i}n\alpha\beta k_m^2}{k_{m-n}^2}f_v^{(n)} - \frac{\mathrm{i}n\alpha\beta}{k_{m-n}^2}f_v^{(n)}\,\mathrm{D}^2\right],\\
\hat{G}_\theta^{(m,n)} &= Re\left[-\frac{1}{k_{m+n}^2}2n\alpha\beta\gamma_{m+n}\left(f_u^{(n)}\right)^*\mathrm{D} - \frac{n\alpha\beta}{k_{m+n}^2}(\gamma_m + \gamma_{m+n})\left(\mathrm{D}f_u^{(n)}\right)^*\right.\\
&\quad \left.+\frac{\mathrm{i}n\alpha\beta k_m^2}{k_{m+n}^2}\left(f_v^{(n)}\right)^* + \frac{\mathrm{i}n\alpha\beta}{k_{m+n}^2}\left(f_v^{(n)}\right)^*\mathrm{D}^2\right],\\
S_v^{(m,n)} &= Re\left[\beta\,\mathrm{D}f_u^{(n)} - \frac{\mathrm{i}n\alpha\beta}{k_{m-n}^2}f_v^{(n)}\,\mathrm{D}^2\right],
\end{aligned}
$$

$$\hat{S}_v^{(m,n)} = Re\left[\beta\left(\mathrm{D}f_u^{(n)}\right)^* + \frac{\mathrm{i}n\alpha\beta}{k_{m+n}^2}\left(f_v^{(n)}\right)^*\mathrm{D}^2\right],$$

$$S_v^{(0)} = -\beta\,\mathrm{D}f_u^{(0)},$$

$$S_\theta^{(m,n)} = Re\left[-\mathrm{i}\gamma_m f_u^{(m)} - \frac{1}{k_{m-n}^2}(\beta^2 + \gamma_m\gamma_{m-n})f_v^{(n)}\,\mathrm{D}\right],$$

$$\hat{S}_\theta^{(m,n)} = Re\left[-\mathrm{i}\gamma_m\left(f_u^{(m)}\right)^* - \frac{1}{k_{m+n}^2}(\beta^2 + \gamma_m\gamma_{m+n})\left(f_v^{(n)}\right)^*\mathrm{D}\right],$$

$$S_\theta^{(0)} = -\mathrm{i}\gamma_m f_u^{(0)}.$$

Appendix B

The kinetic energy is defined by (3.11). We shall begin discussion of its numerical evaluation by starting with the first term in the integrand. It is convenient to write the streamwise disturbance velocity component in the form

$$u_D(x, y, z, t) = \hat{u}(x, y, t)\mathrm{e}^{\mathrm{i}\delta x + \mathrm{i}\beta z} + \hat{u}^*(x, y, t)\mathrm{e}^{-\mathrm{i}\delta x - \mathrm{i}\beta z}. \tag{B 1}$$

where the form of $\hat{u}$ can be easily deduced from (3.4). Evaluation of the energy integral in the spanwise direction results in

$$\int_o^{\lambda_z} u_D^2\,\mathrm{d}z = \int_0^{\lambda_z}(\hat{u}^2\mathrm{e}^{2\mathrm{i}(\delta x+\beta z)} + 2\hat{u}\hat{u}^{*2} + \hat{u}^{*2}\mathrm{e}^{-2\mathrm{i}(\delta \mathrm{i}+\beta z)})\,\mathrm{d}z = 2|\hat{u}|^2\lambda_z. \tag{B 2}$$

Since similar arguments hold for V_D and W_D, the kinetic energy can be written as

$$E_k = \frac{1}{2\lambda_x}\int_0^{\lambda_x}\int_{y_L}^1(|\hat{u}|^2 + |\hat{v}|^2 + |\hat{w}|^2)\,\mathrm{d}y\,\mathrm{d}x \tag{B 3}$$

where $\lambda_x = 2\pi/\alpha$. The above integrals need to be evaluated numerically. Applying transformation defined as

$$x = \xi/\alpha, \quad y = \tfrac{1}{2}[1 - y_L(\xi)]\zeta + \tfrac{1}{2}[1 + y_L(\xi)] \tag{B 4}$$

they become

$$E_k(t) = \frac{1}{8\pi}\int_0^{2\pi}\int_{-1}^1\{|\hat{u}|^2 + |\hat{v}|^2 + |\hat{w}|^2\}[1 + y_L(\xi)]\,\mathrm{d}\zeta\,\mathrm{d}\xi. \tag{B 5}$$

Insertion of the explicit expressions for $\hat{u}$, $\hat{v}$, $\hat{w}$ results in

$$E_k(t) = \frac{1}{8\pi}\sum_{n=-\infty}^{n=\infty}\sum_{m=-\infty}^{m=\infty}\int_0^{2\pi}\int_{-1}^1 h^{(m,n)}(t, \xi, \zeta)[1 + y_L(\xi)]\,\mathrm{d}\zeta\,\mathrm{d}\xi \tag{B 6}$$

where

$$h^{(n,m)}(t, \xi, \zeta) = \left\{\tilde{g}_v^{(m)}\tilde{g}_v^{(n)^*} + k_m^{-2}k_n^{-2}\left[(\gamma_m\gamma_n + \beta^2)\left(D\tilde{g}_v^{(m)}D\tilde{g}_v^{(n)^*} + \tilde{\theta}^{(m)}\tilde{\theta}^{(n)^*}\right)\right.\right.$$
$$\left.\left. - \mathrm{i}\beta(m-n)\alpha\,\mathrm{D}\tilde{g}_v^{(m)}\tilde{\theta}^{(n)^*} - \mathrm{i}\beta(m-n)\alpha\,\mathrm{D}\tilde{g}_v^{(n)^*}\tilde{\theta}^{(m)}\right]\right\}\mathrm{e}^{\mathrm{i}(m-n)\xi}.$$

The coefficients with the tilde refer to the evaluation of the modal functions in the (ξ, ζ)-plane. The required Chebyshev polynomials can be expressed as

$$\hat{T}_j(\xi, \zeta) = \hat{T}_j\left(\tfrac{1}{2}[1 - y_L(\xi)]\zeta + \tfrac{1}{2}[1 - y_L(\xi)]\right) = \hat{T}_j(y(\xi, \zeta)) = T_j\left(\frac{y + S}{1 + S}\right).$$

It is convenient to define matrices $\boldsymbol{E}^{(m,n)}$ made of four sub-blocks. When $n, m \in (-\infty, \infty)$, the range of indices is truncated in the calculations to $(-M, +M)$ as

dictated by the number of Fourier modes retained in the calculations. The top left, bottom left, top right and bottom right sub-blocks are defined as

$$E^{(m,n)}_{j,k} = \frac{1}{4\alpha}\int_0^{2\pi}\int_{-1}^{1}\tilde{T}_j(\xi,\zeta)\,\tilde{T}_k(\xi,\zeta)\,[1-y_L(\xi)]\,\mathrm{e}^{\mathrm{i}(n-m)\xi}\,\mathrm{d}\zeta\,\mathrm{d}\xi + \frac{\gamma_m\gamma_n+\beta^2}{4\alpha\,k_m^2k_n^2}\int_0^{2\pi}\int_{-1}^{1}\mathrm{D}\tilde{T}_j(\xi,\zeta)\,\mathrm{D}\tilde{T}_k(\xi,\zeta)\,\big[1-y_L(\xi)\big]\,\mathrm{e}^{\mathrm{i}(n-m)\xi}\,\mathrm{d}\zeta\,\mathrm{d}\xi, \quad (\mathrm{B}\,7a)$$

$$E^{(m,n)}_{j,K_v+k+1} = -\frac{\mathrm{i}(n-m)\,\beta}{4k_m^2k_n^2}\int_0^{2\pi}\int_{-1}^{1}\mathrm{D}\tilde{T}_j(\xi,\zeta)\,\tilde{T}_k(\xi,\zeta)\,[1-y_L(\xi)]\,\mathrm{e}^{\mathrm{i}(n-m)\xi}\,\mathrm{d}\zeta\,\mathrm{d}\xi, \quad (\mathrm{B}\,7b)$$

$$E^{(m,n)}_{K_v+j+1,k} = -\frac{\mathrm{i}(n-m)\,\beta}{4k_m^2k_n^2}\int_0^{2\pi}\int_{-1}^{1}\tilde{T}_j(\xi,\zeta)\,\mathrm{D}\tilde{T}_k(\xi,\zeta)\,[1-y_L(\xi)]\,\mathrm{e}^{\mathrm{i}(n-m)\xi}\,\mathrm{d}\zeta\,\mathrm{d}\xi, \quad (\mathrm{B}\,7c)$$

$$E^{(m,n)}_{K_V+j+1,K_v+k+1} = \frac{\gamma_m\gamma_n+\beta^2}{4\alpha\,k_m^2k_n^2}\int_0^{2\pi}\int_{-1}^{1}\tilde{T}_j(\xi,\zeta)\tilde{T}_k(\xi,\zeta)\,[1-y_L(\xi)]\,\mathrm{e}^{\mathrm{i}(n-m)\xi}\,\mathrm{d}\zeta\,\mathrm{d}\xi, \quad (\mathrm{B}\,7d)$$

respectively, where $j=0,\ldots,K_v$, $k=0,\ldots,K_\theta$. The above integrals are evaluated numerically with spectral accuracy using Gauss–Chebyshev and trapezoidal (Isaacson & Keller 1966) methods in the ζ- and ξ-directions, respectively. The kinetic energy can be evaluated as

$$E_k = \boldsymbol{\eta}^H\boldsymbol{E}\boldsymbol{\eta} \quad (\mathrm{B}\,8)$$

where the matrix $\boldsymbol{E}$ has the form

$$\boldsymbol{E} = \begin{bmatrix} E^{(-M,-M)} & \cdots & E^{(-M,0)} & \cdots & E^{(-M,M)} \\ \vdots & \vdots & \vdots & \vdots & \vdots \\ E^{(0,-M)} & \cdots & E^{(0,0)} & \cdots & E^{(0,M)} \\ \vdots & \vdots & \vdots & \vdots & \vdots \\ E^{(M,-M)} & \cdots & E^{(M,0)} & \cdots & E^{(M,M)} \end{bmatrix}, \quad (\mathrm{B}\,9)$$

$\boldsymbol{\eta}$ stands for the vector of unknown coefficients of the Chebyshev expansions defined in (4.2) and $2M+1$ denotes the number of Fourier modes retained in the solution.

REFERENCES

Bradshaw, P. 2000 A note on "critical roughness" and "transitional roughness". *Phys. Fluids* **12**, 1611–1614.

Butler, M. & Farrell, B. F. 1992 Three-dimensional optimal perturbations in viscous shear flow. *Phys. Fluids* A **4**, 1637–1650.

Colebrook, C. F. 1939 Turbulent flow in pipes, with particular reference to the transition region between smooth and rough pipes. *J. Inst. Civ. Engng* **11**, 133–156.

Corke, T. C., Bar Sever, A. & Morkovin, M. V. 1986 Experiments on transition enhancements by distributed roughness. *Phys. Fluids* **9**, 3199–3213.

Darcy, H. 1857 *Recherches Expérimentales Relatives au Mouvement de l'Eau dans les Tuyaux*. Paris, Mallet-Bachelier.

DiPrima, R. C. & Habetler, G. J. 1969 A completeness theorem for non-selfadjoint eigenvalue problems in hydrodynamic stability. *Arch. Rat. Mech. Anal.* **32**, 218–227.

Floryan, J. M. 1997 Stability of wall-bounded shear layers in the presence of simulated distributed surface roughness. *J. Fluid Mech.* **335**, 29–55.

Floryan, J. M. 2002 Centrifugal instability of Couette flow over a wavy wall. *Phys. Fluids* **14**, 312–322.

Floryan, J. M. 2003 Vortex instability in a diverging-converging channel. *J. Fluid Mech.* **482**, 17–50.

Floryan, J. M. 2004 Three-dimensional instabilities of laminar flow in a rough channel and the concept of hydraulically smooth wall. *Expert Systems in Fluid Dynamics Research Laboratory Rep. ESFD*-3/2004. Department of Mechanical and Materials Engineering, The University of Western Ontario.

Floryan, J. M. 2005 Two-dimensional instability of flow in a rough channel. *Phys. Fluids* **17**, 044101/8.

Hagen, G. 1854 Uber den Einfluss der Temperatur auf die Bewegung des Wasser in Röhren. *Math. Abh. Akad. Wiss., Berlin*, pp. 17–98.

Isaacson, E. & Keller, H. B. 1966 *Analysis of Numerical Methods*. Wiley.

Jimenez, J. 2004 Turbulent flows over rough walls. *Annu. Rev. Fluid Mech.* **36**, 173–196.

Moody, L. F. 1944 Friction factors for pipe flow. *Trans. ASME* **66**, 671–684.

Nikuradse, J. 1933 Strömungsgesetze in Rauhen Rohren. *VDI-Forschungscheft* 361 (also NACA TM 1292 (1950)).

Reddy, S. C. & Henningson, D. S. 1993 Energy growth in viscous channel flows. *J. Fluid Mech.* **252**, 209–238.

Reynolds, O. 1883 An experimental investigation of the circumstances which determine whether the motion of water shall be direct or sinuous, and of the wall of resistance in parallel channels. *Phil. Trans. R. Soc. Lond.* **174**, 935–982.

Reshotko, E. 1984 Disturbances in a laminar boundary layer due to distributed surface roughness. In *Turbulence and Chaotic Phenomena – Proc. IUTAM Symp.* (ed. T. Tatsumi), pp. 39–46. Elsevier.

Schlichting, H. 1979 *Boundary Layer Theory*, 7th Edn. McGraw-Hill.

Schmid, P. J. & Henningson, D. S. 2001 *Stability and Transition in Shear Flows*. Springer.

Szumbarski, J. & Floryan, J. M. 1999 A direct spectral method for determination of flows over corrugated boundaries. *J. Comput. Phys.* **153**, 378–402.

Szumbarski, J. 2002 Immersed boundary approach to stability equations for a spatially periodic viscous flow. *Arch. Mech.* **54**, 199–222.

Trefethen, L. N., Trefethen, A. E., Reddy, S. C. & Driscoll, T. A. 1993 Hydrodynamic stability without eigenvalues. *Science* **261**, 578–584.

Waigh, D. R. & Kind, R. J. 1998 Improved aerodynamic characterization of regular three-dimensional roughness. *AIAA J.* **36**, 1117–1119.